Stable, unstable, and defected confined states of traveling-wave convection

Paul Kolodner
AT&T Bell Laboratories, Murray Hill, New Jersey 07974-0636
(Received 23 February 1994)

I describe an extensive experimental study of the structure, propagation, and stability of one-dimensional confined states of traveling-wave convection in ethanol-water mixtures in an annular convection cell. The widths of these confined states are found to form a discrete set in parameter space. The principal difference between wide and narrow confined states lies in their *dynamical stability:* wide confined states are unstable for $\psi \gtrsim -0.13$ and can only be maintained in a steady state using active servo control, whereas narrow "pulses" are stable for all separation ratios studied. These observations are in qualitative agreement with the predictions of a complex-Ginzburg-Landau-equation model and in disagreement with previous observations of a continuum of confined-state widths at separation ratio $\psi = -0.25$. These experiments also document new confined states, including one in which lines of spatiotemporal dislocations separate slow and fast traveling waves.

PACS number(s): 47.27.Te, 47.20.Bp, 47.20.Ky

I. INTRODUCTION

One of the most intriguing aspects of traveling-wave (TW) convection in binary fluid mixtures is the existence of *confined states:* spatially localized convecting regions which are surrounded by quiescent fluid. Stable confined states whose width was ≈ 5 times the height of the experimental cell were first observed at separation ratio $\psi = -0.08$ in the one-dimensional geometry defined by a narrow, rectangular convection cell [1]. Subsequently, very wide confined states were observed in experiments using a fluid with $\psi = -0.25$ in a long, narrow annulus [2]. Dynamical confined states which "blink" back and forth across a narrow rectangular cell have been studied in great detail at small $|\psi|$ [3]. Finally, experiments in very wide cells have demonstrated the existence of two-dimensional confined states for a range of separation ratios [4].

Interest in this subject has focused mainly on the narrow confined states, first observed for $\psi = -0.08$ in Ref. [1], rather than on the wider structures seen at more negative ψ. One reason for this is that the spatial structure of narrow confined states bears a strong resemblance to that of "pulse" solutions of the complex Ginzburg-Landau equation (CGLE), which is often used to model this system [5–8]. Another reason is the ubiquity of experimental "pulses": they are the first convective state seen above onset over a wide range of ψ, they persist over a finite range of Rayleigh number r near onset, and their spatial structure varies weakly with ψ and r. TW pulses are in fact rather difficult to avoid in experiments on this system. Extensive experimental study has been directed at clarifying the issues of existence and structure [9–11], drift [10,12], stability [10,13–15], and collisions [16] of TW pulses. Theoretical understanding of these observations has advanced via numerical and analytical work on the CGLE [5–8,17], by the extension of this model to include the effects of "self-trapping" of pulses by their own convective concentration field [18], and through numerical integration of the full Navier-Stokes equations [19].

The wide confined states observed at more negative ψ have received comparatively less theoretical and experimental attention. This is partly because of our intuition that the "weakly nonlinear" CGLE model becomes less and less relevant to the "strongly nonlinear" experimental behavior that is encountered as ψ is made more negative. Indeed, the spatial structure of these states has so far been accounted for in detail only by numerical integrations of the full fluid equations [19,20]. More importantly, however, the qualitative behavior of these wide confined states exhibited two features which directly contradict the predictions of the CGLE model: they did not drift, and they exhibited a continuous family of widths. In the experiments reported in Ref. [2], motionless, stable confined states of any desired width could be maintained for any Rayleigh number inside a "locking band" of width 2.3%. [Another way to say this is that the subset of the (r,w) plane on which time-independent confined states were seen consisted of a continuous, two-dimensional area.] For this reason, these wide states were given the designation "arbitrary width." But the existence of a continuum of confined-state widths over a finite range of parameters is not consistent with the CGLE; in this model, pulse solutions form a discrete, countable set [6]. On this basis, one would expect to find that the subset of the (r,w) plane on which time-independent confined states are seen at a fixed separation ratio consists of a set of measure zero: a curve or a group of points. Furthermore, in a system with continuous translational symmetry, the drift velocity of pulse solutions to the CGLE vanishes only for a set of parameters which has measure zero. Thus arbitrary-width confined states which were motionless over range of Rayleigh numbers appeared anomalous, both in the context of the CGLE model and in comparison with the experimental behavior of narrow pulses at less negative separation ratio.

Thus there remain several important open questions in

our understanding of one-dimensional confined states of TW convection: (1) What is the relationship between wide and narrow confined states? (2) What are their domains of existence in parameter space? Do these domains overlap? (3) Why do arbitrary-width confined states not drift, and why is there a locking band? (4) Are there other time-independent confined states which have not yet been observed?

This paper addresses these questions through a series of experiments on fluids with $\psi=-0.127$, -0.167, -0.210, and -0.253 in a narrow, extremely uniform, annular convention cell. From the results of these experiments, a simple, comprehensive picture has emerged: For any ψ in a wide range of separation ratios, confined states of any width w greater than about 5 times the cell height can be observed. All confined states drift through the cell at constant velocity $v_{\rm dr}$; $v_{\rm dr}$ is a continuous function of parameters which vanishes only on a set of measure zero. The observed dynamics of confined states of all widths can be expressed in terms of a differential equation for the confined-state width:

$$\tau_o \frac{dw}{dt} = r - r_o(w) \ . \tag{1}$$

Here $\tau_o(w)>0$ is a characteristic time and $r_o(w)$ is the *neutral Rayleigh number* at which a confined state of width w neither grows nor shrinks in space. The quantitative results presented in this paper consist of the measurement of $\tau_o(w)$ and of $r_o(w)$ at several separation ratios. As explained in Sec. III below, the function $r_o(w)$ expresses the *dynamical stability* of the confined states, and herein lies the principal reason why wide and narrow confined states have previously been seen only at different separation ratios: wide confined states are stable for $\psi \leq -0.167$, but at smaller $|\psi|$, they are unstable and can only be maintained using active servo control. Narrow confined states are stable and easily observable at all ψ studied.

The widths of the time-independent confined states observed in these experiments form a discrete set in parameter space. What this means experimentally is that, for a given ψ, the equation $dw/dt=0$ is satisfied only on a measure-zero subset—a curve—of the (r,w) plane. Examples of such curves are given in Fig. 32 below. In contrast, the "locking band" described in Ref. [2] is a two-dimensional region in this plane: a strip of finite width in both r and w. The experimental situation documented in this work is qualitatively consistent with the picture that emerges from the study of simple solutions of the CGLE [6–8].

Along with the locking band, the lack of drift described for wide confined states in Refs. [2,20] has also not been reproduced in the present work. The major reason for this is that, for $-0.25 \lesssim \psi \lesssim -0.19$, the drift velocity of wide confined states is very small and almost independent of Rayleigh number. Thus these structures are easily pinned by weak, local inhomogeneities in the experimental cell; once pinned, it takes a large change in Rayleigh number to unpin them again. Avoiding this artifactual behavior has required the development of an extremely uniform convection cell.

The final observations in this work demonstrate that there is indeed a type of persistent confined state which has not been previously documented: a weakly unstable, *defected confined state* in which regions of slow and fast TW coexist, separated by lines of spatiotemporal dislocations.

The rest of this paper is organized as follows. The apparatus and procedures used in these experiments are described in Sec. II. The model presented in Eq. (1) above for the evolution of confined states is discussed further in Sec. III and its application to data analysis is described. Stable and unstable confined states observed at $\psi=-0.127$ are described in Sec. IV. Section V contains observations of wide confined states for $\psi=-0.253$; a preliminary version of some of these results has already appeared in Ref. [21]. Sections VI and VII contain detailed characterizations of confined states of all widths at $\psi=-0.210$ and -0.167, respectively. New confined states observed at $\psi=-0.127$ and -0.167 are described in Sec. VIII. A summary and discussion follow in Sec. IX.

II. APPARATUS AND PROCEDURES

The apparatus and techniques used in these experiments have been extensively described in recent publications [10,16,22,23]. The cell is an annular channel of height $d=0.2737$ cm, radial width $1.677d$, and mean circumference $82.47d$, formed by a concentric plastic disk and ring which are clamped between an electrically heated, mirror-polished silicon bottom plate and a transparent, water-cooled sapphire top plate. The long- and short-term fractional stability of the applied vertical temperature difference is 5×10^{-5}. By means of 24 adjustable trim heaters arranged in a circle on the underside of the bottom plate of the cell, and using the pulse-drift technique described in Refs. [10,16], the spatial profile of the applied temperature difference can be measured and made uniform to within 4×10^{-4}. These trim heaters can also be used to deliberately apply strongly nonuniform heating of the bottom plate.

The flow patterns produced in this cell are viewed by a shadow graphic flow-visualization system and are recorded by an annular array of 720 photodiodes under the control of a small computer. These patterns consist of radial wave fronts which propagate azimuthally around the cell under a spatially localized amplitude profile. The principal analysis of the data consists of the calculation of the amplitude and wave-number profiles by demodulation in space at the measured mean wave number, using the techniques described in Refs. [22,23]. The precision of these calculations is at the 1% level. All of the flow visualizations reported in this paper were made with the same settings of the optical system, so that TW amplitude profiles for confined states at different separation ratios can be compared directly. While these computations are usually done off line to take advantage of the properties of noncausal digital filters, it has also been useful to perform real-time demodulation for monitoring and controlling the widths of confined states. These procedures will be discussed in Sec. III below. In addition to the calcula-

tion of amplitude and wave-number profile, temporal demodulation at each spatial point in the shadowgraph image has been used to produce spatial maps of the oscillation frequency for selected data sets. Finally, TW phase velocities and amplitude-profile drift velocities have been measured either from the computered wave-number, amplitude, and oscillation-frequency profiles or, in cases where less precision is required, simply by laying a ruler on graphs of the space-time trajectories of TW roll boundaries and of the leading and trailing edges of confined-state amplitude profiles. The signs of drift velocities are defined with respect to the direction of propagation of the underlying TW's, and all of the demodulated wave-number and amplitude profiles presented in this paper have been plotted so that the TW's propagate to the right.

The fluids used in these experiments are aqueous solutions of ethanol whose thermophysical properties are listed in Table I [24]. Table I also lists some landmark Rayleigh numbers. It should be noted that the Rayleigh numbers quoted herein for experiments on confined states at $\psi=-0.127$ have been calibrated exactly against the Rayleigh numbers measured in Ref. [22]. As usual, the Rayleigh numbers quoted in this paper have been normalized to the calculated critical Rayleigh number for the onset of convention in a pure fluid in an infinite system; such "reduced Rayleigh numbers" are symbolized by a lowercase r. As is also usual, I have scaled lengths with the cell height d, velocities with d/τ_v, and frequencies with τ_v^{-1}, where the vertical thermal-diffusion time τ_v is listed for each experimental fluid in Table I.

It is useful to define a few points of nomenclature used in this paper. The term "confined state" will be given generically to any slowly varying TW structure which does not fill the experimental cell. The word "pulse" is generally used to describe strongly stable confined states of widths between 4 and 6 times the cell height; the meaning of the term "strongly stable" is made clear below. The repeated exception to this rule concerns wide "unstable pulses," which are described in Sec. IV. "Extended states" are patterns of spatially uniform amplitude which fill the entire experimental cell.

I conclude this section with a discussion of the major sources of uncertainty in the Rayleigh numbers, which are somewhat different for confined-state experiments than for the extended-state observations in Ref. [22]. There are four: slow drifts, new uncertainties in the computation of the Rayleigh number from the experimentally applied temperature difference, spatial nonuniformities, and absolute uncertainties.

As described in Ref. [22], long-term measurements in this system are subject to small Rayleigh-number drifts which appear to be caused by a slow decrease in the concentration of the experimental fluid. These drifts are so small that they can be monitored by repeated measurement of the oscillation frequency of extended states of TW's and compensated by applying a time-dependent Rayleigh-number correction. This polynomial correction is adjusted by minimizing the rms deviation of the ensemble of frequency measurements from a heavily smoothed spline fit. In the present work, observations of confined states were interspersed with many such TW frequency measurements and the optimized drift correction was applied to the Rayleigh numbers recorded for the confined-state measurements. The fractional drift rates observed here were smaller than those reported in Ref. [22]—$(0.3-0.5)\times10^{-4}$ per day, maximum drift correction 0.003—and the rms deviation of the frequency measurements from the smoothed spline fit corresponded to a Rayleigh-number uncertainty of $\pm(1.6-1.8)\times10^{-4}$, depending on ψ.

Reference [22] also contained a discussion of the procedure used to convert the experimentally applied temperature differences into Rayleigh numbers. This is accomplished by computing the temperature field inside the experimental cell, using a numerical integration of the heat equation which assumes azimuthal symmetry. The computation incorporates the geometry of the cell and the thermal properties of the materials used in its construction, as well as a heuristic model for convective heat transport by spatially uniform states of nonlinear TW's. The uncertainties in this model caused a relative uncertainty of $\pm1\times10^{-4}$ in the Rayleigh numbers computed for different extended states of nonlinear TW's at the same separation ratio. However, extending this model to confined states of TW's presents two problems. First, the

TABLE I. Fluid parameters and Rayleigh-number landmarks. Conc. denotes the ethanol concentration by weight. T_{mean} is the temperature in degrees Celsius at midheight in fluid layer. The absolute uncertainty is $\sim0.03\,^{\circ}$C. ψ, P, and L are the separation ratio, Prandtl number, and Lewis number, respectively, from Ref. [24]. τ_v is the vertical thermal-diffusion time in seconds. The approximate absolute uncertainties in ψ, P, L, and τ_v are 1.5%, 3%, 5%, and 2%, respectively. Relative uncertainties in all of these parameters are probably $\lesssim1\%$. r_s is the saddle-node Rayleigh number, below which extended states of nonlinear TW lose stability to the conductive state. $r_o(w=12)$ is the Rayleigh number at which a confined state of width 12 neither grows nor shrinks in space. r_{co} is the threshold at which the quiescent state loses stability to small-amplitude traveling waves.

Conc.	T_{mean}	ψ	P	L	τ_v	r_s	$r_o(w=12)$	r_{co}
0.028	27.51	−0.127	6.862	0.0083	52.6	1.226 43(10)	1.300 2(8)	1.291 33(36)
0.040	27.68	−0.167	7.309	0.0083	53.2	1.241 4(8)	1.307 4(4)	1.348 79(10)
0.056	27.81	−0.210	7.932	0.0082	54.2	1.279 3(5)	1.336 89(22)	1.429 87(16)
0.080	27.82	−0.253	8.929	0.0079	55.6	1.242 1(8)	1.337 45(24)	1.460 23(17)

localized heat transport by confined states breaks the azimuthal symmetry of the calculation. Worse, our understanding of the heat transport by confined states is even more sketchy than that for extended states. The simplest *ad hoc* solution to this problem is to continue to model this situation with an azimuthally symmetric computation, equating the local heat transport by a confined state of mean wave number k_m with that by an extended state of that wave number. However, this solution is not feasible, because the values of k_m measured for the confined states in this paper are too high: their (Rayleigh-number, wave-number) coordinates lie far outside the Eckhaus boundary for extended states of TW's, and the heat-transport model accordingly predicts no convective heat transport for such states. In order to obtain a physically reasonable number for the convective heat transport, I modified the numerical model to compute the heat transport by the extended state whose wave number is approximately equal to the mean of k_m and the saddle-node wave number k_E. The uncertainty introduced by this approximation is estimated to be $\pm(2.6-3.5)\times10^{-4}$, depending on ψ. The heat-transport model also depends on the saddle-node Rayleigh number r_s listed in Table I, but this dependence is so weak that is has not been necessary to measure r_s with a precision much better than 0.001.

In addition to the enhanced uncertainty of the Rayleigh-number calculation, confined-state measurements suffer from uncertainties due to spatial nonuniformities in the apparatus which would be averaged away quite effectively in an extended TW state. The confined-state measurements in this paper were all performed in a particularly uniform section of the cell; the spatial variation of the Rayleigh number in this section was found from pulse-drift measurements at $\psi=-0.127$ to be $\delta r=\pm3.5\times10^{-4}$. To account for the spatial averaging that is undoubtedly felt by wide confined states, I have estimated the uncertainty due to spatial nonuniformity as $\delta r(w_p/L_{CS})^{1/2}$, where $w_p=5.5$ is the width of the TW pulse used to measure that spatial Rayleigh-number profile and L_{CS} is the total extent of the cell traversed by the confined state under study during a given measurement. This spatial averaging reduces the additional Rayleigh-number uncertainty to as little as $\pm(1.2-1.5)\times10^{-4}$ for confined states which traverse a very wide section of the experimental cell.

Finally, the absolute uncertainty of the Rayleigh numbers quoted in this paper is estimated to be $\pm2\%$ [22]. However, since the ethanol concentrations used in this work all lie in a rather narrow range, I would expect that the relative uncertainty of Rayleigh numbers measured at different separation ratios would be quite a bit less than this rather high absolute uncertainty. In Ref. [22], I found that Rayleigh numbers measured at identical applied temperature differences with separately prepared experimental fluids of nominally identical concentration differed by $\lesssim0.003$. These differences were attributed to the accuracy with which the ethanol concentration could be reproduced when preparing a new fluid. This number also coincides with the maximum drift correction applied in the present work and thus represents a lower bound for the relative uncertainty of Rayleigh numbers measured at different separation ratios.

In light of these remarks, the Rayleigh numbers quoted in this paper are subject to a hierarchy of uncertainties:

(i) Comparisons between different extended states observed at the same separation ratio suffer from relative uncertainties of $(1.4-2.1)\times10^{-4}$, as in Ref. [22].

(ii) Comparisons between confined states of different widths at the same separation ratio exhibit relative uncertainties of $(2.6-5)\times10^{-4}$. The error bars in the figures below all fall into this range.

(iii) Comparisons between measurements at different separation ratios exhibit relative uncertainties of about ±0.003.

(iv) The absolute uncertainty of the Rayleigh numbers quoted in this paper is of the order $\pm2\%$.

III. MODELING AND CONTROLLING CONFINED-STATE DYNAMICS

Confined states tend to expand in space when the Rayleigh number r is increased and to shrink when r is decreased. The time scale of this evolution and the Rayleigh-number range over which this observation is valid depend on the confined-state width w and the separation ratio ψ. This qualitative picture is mirrored in the simple model of confined-state dynamics given in Eq. (1) above. This equation has proven to be an accurate description of most of the observations presented in this paper and has allowed for the experimental control of previously unstudied unstable confined states. Most of the experiments in this paper consist of measuring the confined-state expansion velocity $\Delta v=dw/dt$ as a function of Rayleigh number and width. Most of the data analysis consists of fitting such measurements to Eq. (1) so as to deduce the dependences of $r_o(w)$ and $\tau_o(w)$ on w and ψ.

The simplest application of Eq. (1) to data analysis is to make measurements of the Rayleigh-number dependence of Δv for a narrow range of widths near some mean width $\bar{w}$. If this range of widths is sufficiently narrow, it turns out that the width dependence of τ_o is unimportant and that $r_o(w)$ is well approximated by a linear function of w. Thus fitting the measurements of $\Delta v(r,w)$ to a bilinear form

$$\Delta v=\alpha r+\beta(w-\bar{w})-\delta \tag{2}$$

by adjusting the parameters α, β, and δ, I obtain $\tau_o=1/\alpha$, $r_o(w=\bar{w})=\delta/\alpha$, and $dr_o/dw=-\beta/\alpha$. This is the basic idea of the analysis used in this paper.

Two extensions of this fit procedure are used in some of the analysis in this work. In Sec. V below, the measurements of Δv are made over quite a wide range of r and it turns out that they deviate very slightly from a linear dependence on r. To account for this, parabolic and cubic terms in r are added to the fit of Eq. (2). The linear model of Eq. (1) is accurate only for small values of $r-r_o(w)$. In Sec. VI below, measurements are made over a narrow range of $r-r_o(w)$, but over a range of w that is so wide that the width dependence of $\tau_o(w)$ must be taken into account, and the assumption that $r_o(w)$ is linear in w cannot be made (see Fig. 15 below). I started the

analysis in this case by parametrizing $\tau_o(w)$ as a linear function of w. Rather than assume a particular form for the width dependence of $r_o(w)$, I used a spline fit to extract $r_o(w)$ as well as the parameters describing $\tau_o(w)$. The details of this fit procedure are given in Sec. VI.

The stability properties of Eq. (1) are crucial in understanding and controlling confined-state evolution. Suppose that $w(t)=w_r$ is the time-independent solution of Eq. (1) for a given Rayleigh number r. Expanding about this solution gives

$$\frac{d\delta w}{dt}=-\tau_o^{-1}\frac{dr_o}{dw}\delta w+\cdots , \tag{3}$$

where $\delta w=w(t)-w_r$ is the deviation from the steady-state width. Confined states for which the dimensionless growth rate $\gamma=-\tau_o^{-1}(dr_o/dw)<0$ are *dynamically stable*. For small negative γ, such states relax slowly towards the steady-state width. Fits to Eq. (1) describe such dynamics with quantitative accuracy, even if the steady-state width is not reached experimentally. However, in Sec. IV below, I describe wide confined states for which γ is strongly positive. These *dynamically unstable* confined states either grow to fill the entire cell with TW's or else they shrink in width, evolving into narrow pulses (for which $\gamma<0$). This unstable evolution is so fast that meaningful observations cannot be made in uncontrolled experiments. In order to maintain these structures in a time-independent state, it has been necessary to use active servo control based on Eq. (1). The scheme of this control is quite simple. Beginning with an estimate for $\tau_o(w)$, a measurement of Δv is made at a particular Rayleigh number. The observation that a confined state of width w exhibits an expansion velocity Δv at Rayleigh number r implies that the neutral Rayleigh number at this width is $r_o(w)=r-\tau_o\Delta v$, according to Eq. (1). Changing r to this value should cause Δv to vanish. Applying this measurement-and-correction sequence repeatedly should keep the confined-state width constant.

These ideas have been implemented in an experimental servo control program which stabilizes the pulse width at any desired value w_t and provides estimates of the neutral Rayleigh number $r_o(w_t)$. For this purpose, the flow-visualization computer acquires shadowgraph data repeatedly, computes the spatial TW amplitude profile in real time, locates the 50%-amplitude points in this profile, and produces an analog signal proportional to their difference w. The computer which controls the Rayleigh number digitizes this signal, forming a time series. At successive times separated by $\delta t=1200-1800$ sec, the latest segment of this time series is fit to a straight line, yielding estimates for the expansion velocity Δv and for the average pulse width $w_{\rm av}$. Then, the Rayleigh number r is changed to $r-\tau_o[\Delta v+(w_f-w_t)/\delta t]$, where $w_f=w_{\rm av}+\Delta v\delta t/2$ is the width at the end of the latest time segment. This adjustment corrects both for the nonzero expansion velocity Δv and for the width error w_f-w_t. The program also records the values of r, Δv, and $w_{\rm av}$ for each time period, to allow later computation of $r_o(w_{\rm av})=r-\tau_o\Delta v$. Because Δv is kept small, the accuracy of this estimate is insensitive to the uncertainty in τ_o.

Experimentally, it is found that this servo has a tendency to ring when applied to the strongly unstable confined states studied in Sec. IV below. Part of this ringing was initially due to misadjustment of the overall servo gain (i.e., to the inaccuracy in the measured value of τ_o). However, much of the reason for the ringing appears to be because the system actually has inertia in this dynamical state, i.e., a second-derivative term is missing from Eq. (1). Adding a term proportional to d^2w/dt^2 to the Rayleigh-number correction reduced the ringing substantially. With this control, accurate measurements of the spatiotemporal structure of strongly unstable confined states has been possible.

While the width-control servo has been crucial in making steady-state observations of unstable confined states, it has also been quite useful for studying *stable* confined states as well. This is because the control program produces direct measurements of $r_o(w)$ which do not require accurate knowledge of $\tau_o(w)$. Servo-controlled measurements of $r_o(w)$ were used to supplement the fits based on Eq. (2) above for some of the stable-confined-state measurements described below. The model of Eq. (1) has been found to quantitatively describe the evolution of all the wide, stable confined states encountered in this work.

IV. STABLE AND UNSTABLE PULSES $\psi=-0.127$

Measurements of the spatiotemporal structure of narrow TW pulses over the separation-ratio range $-0.123\le\psi\le-0.030$ have been published by several research groups [9–11]. In Ref. [10], I additionally measured pulse drift for $-0.123\le\psi\le-0.072$. Pulses drift slowly through a sufficiently uniform cell at a velocity $v_{\rm dr}$ whose dependence on Rayleigh number could be accurately fit to a functional form $v_{\rm dr}=v_0+a(r-r_0)^{1/2}$ (pulses are not observed for Rayleigh numbers below a threshold r_2 which is greater than r_0). The structure and drift of narrow pulses studied at $\psi=-0.127$ in the present experiments conform precisely to this picture. With fit coefficients $v_0=-0.040(10)$, $a=0.687(35)$, and $r_0=1.2677(20)$, this function matches the pulse-drift data shown in Fig. 1(a) to within $\delta v=7\times10^{-4}$ rms. Figure 1(b) shows that the TW phase velocity decreases with Rayleigh number; the typical value $v_{\rm ph}\sim0.75$ can be compared with phase velocity 2.4967 exhibited by linear TW's exactly at onset.

The range of Rayleigh numbers over which pulses are stable has also been the subject of extensive experimental study. To set the stage for the present measurements, it will be useful to give a brief survey of this subject here. A detailed discussion is deferred until Sec. IX below. Pulses lose stability and decay when r is reduced below a ψ-dependent threshold denoted r_2 [25]. Increasing r also causes pulses to lose stability, this time by growing in space and filling the cell with TW's. The mechanism which causes this destabilization and the Rayleigh number at which it occurs depend sensitively on the separation ratio and on the conditions of the experiment

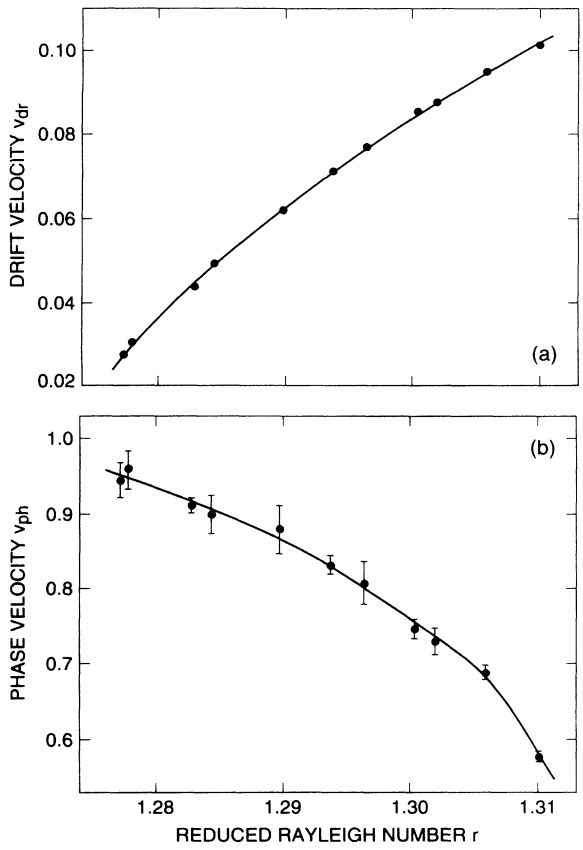

FIG. 1. (a) The drift velocity v_{dr} and (b) the phase velocity v_{ph} are shown as functions of the reduced Rayleigh number r for stable pulses of width 5.0–6.2 at separation ratio $\psi=-0.127$. The Rayleigh-number dependence of the pulse width can be seen in Fig. 5 below. The solid curve in (a) is a fit to the square-root form given in the text; the rms residual of this fit is $\delta v=7\times10^{-4}$. The error bars in this graph are smaller than the symbols. The solid curve in (b) is a guide to the eye. The error bars here are due to the spatial variation of the phase velocity over the width of the pulse.

[10,13–15]. For experiments with $\psi\gtrsim-0.14$, the Rayleigh-number range of pulse existence extends above the onset of convection, where small-amplitude TW fluctuations are convectively amplified. In very long cells, these fluctuations can grow to such high amplitudes that they destroy TW pulses, causing a transition to a cell full of TW's [13]. This is the normal mechanism of pulse destabilization in long cells and small $|\psi|$. However, it is always possible to suppress such fluctuations and reveal other mechanisms of pulse destabilization. In the experiments at $\psi\gtrsim-0.06$ in Ref. [15], fluctuation suppression was accomplished by using rectangular cells that were too short for fluctuations to grow to appreciable amplitude. In those experiments, pulse destabilization was caused by the transition from a convective to an absolute instability, at a threshold denoted r_a. In experiments in a very long annular cell at $\psi=-0.072$, extra pulses were used to absorb TW fluctuations [10]. In that case, the convective-absolute transition was preceded at $r_1<r_a$ by a process that I called "intrinsic destabilization": the pulse simply expanded in space, accompanied by a large decrease in the TW phase velocity. This process was illustrated for $\psi=-0.072$ in Fig. 20 of Ref. [10], in which a pulse underwent destabilization as it drifted through a region of elevated Rayleigh number in a slightly inhomogeneous cell. The pulses which absorbed TW fluctuations in that experiment were placed at regions in the cell where $r<r_1$, so that they remained stable.

The intrinsic destabilization events documented in Ref. [10] were transients observed in an inhomogeneous system in the presence of other pulses. Figures 2 and 3 show analogous events in successively closer approximations to the destabilization of an isolated pulse in a uniform system. In Fig. 2, two pulses lose stability simultaneously after the Rayleigh number is increased from $r=1.312\,77$ to $1.314\,06$. Both pulses expand and suffer a large decrease in phase velocity. Subsequent decreases in the Rayleigh number far below the convective onset, detailed in the figure caption, did not arrest this evolution, and an extended state of TW's was the final result. Interestingly, the trailing edges of both pulses were essentially stationary during the destabilization process and the leading edges advanced at the phase velocity of the underlying

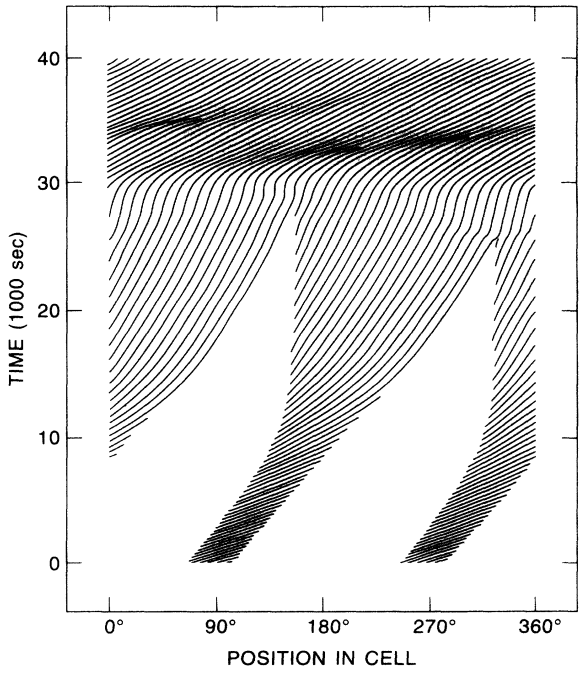

FIG. 2. Space-time plot showing the evolution of a pair of TW pulses at $\psi=-0.127$ which lose stability above threshold $r_1=1.3132(6)$. At time $t=0$ in this run, the Rayleigh number was increased from $r=1.312\,77$ to $1.314\,06$. In response, both pulses began to expand in space, accompanied by a decrease in the TW phase velocity. Subsequent reductions of the Rayleigh number to $r=1.311\,47$ at time $t=14\,240$ sec and to $r=1.299\,90$ at $t=17\,760$ sec did not arrest this process. The expansion of the TW pulses caused the cell to be filled with 42 pairs of rolls, which were then transformed into a right-going, 39-roll-pair state by further reducing the Rayleigh number to $r=1.244\,72$ at about $t=29\,280$ sec.

TW. The intrinsic-destabilization threshold in this system is measured to be $r_1 = 1.3132(6)$. I have not located the lower stability threshold r_2 in these experiments, but the measurements in Ref. [10] imply $r_2 = 1.2692(4)$.

Since $r_1 > r_{co} = 1.291\,33(36)$, TW fluctuations are convectively amplified in this system. Because the experimental cell is so long, some way to absorb these fluctuations must be provided if intrinsic destabilization is to be observed. The obvious way to accomplish this is to use a second pulse, as in Fig. 2. However, once one pulse of a pair has been destabilized and the Rayleigh number has been reduced below onset, TW fluctuations are no longer amplified and the second pulse can be removed. This is what is done in Fig. 3. At the beginning of this run, a well-developed pulse existed at location 130°, and a second pulse was created at location 320° by launching a disturbance from location 90°. The uniformity of the heating of the bottom plate of the cell was then adjusted so that local Rayleigh number in the vicinity of the right-hand pulse exceeded the threshold r_1 while that near the left-hand pulse remained below r_1. Because of this strong gradient, the right-hand pulse lost stability and grew in width, while the left-hand pulse remained too weak to grow, but not too weak to absorb TW fluctuations. After the TW phase velocity and width of the right-hand pulse had been clearly destabilized—near time $t = 8000$ sec—the applied temperature difference was reduced in order to eliminate the pulse on the left. Then, near time $t = 14\,000$ sec, the Rayleigh-number gradient was removed, leaving an isolated, "intrinsically destabilized" pulse in a spatially uniform system. Notice that this structure differs from those produced in Fig. 2. Here both the leading and trailing edges drift in the same direction as the underlying TW, but at a much slower velocity. I will return to the destabilized structures in Fig. 2 in Sec. VIII below.

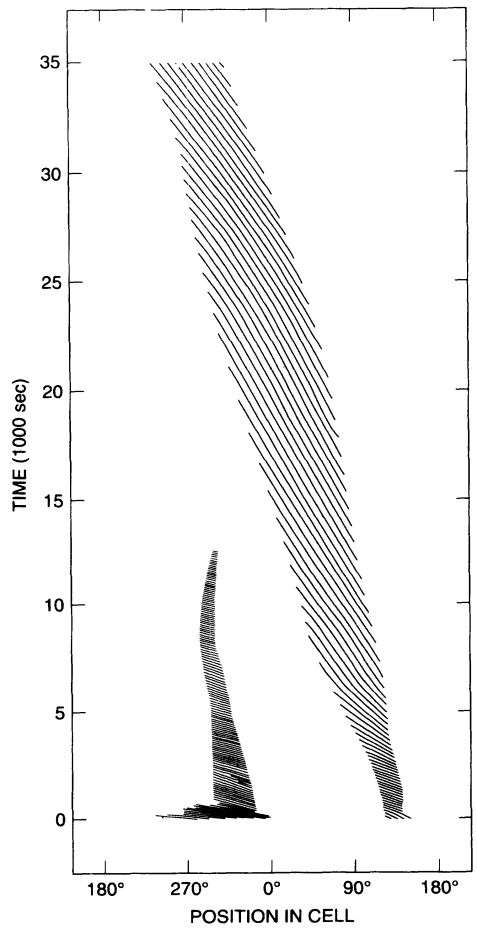

FIG. 3. This space-time plot shows the production of an isolated "unstable pulse" at $\psi = -0.127$. The run began with two narrow pulses; at time $t = 0$, a strong Rayleigh-number gradient was applied, causing the pulse on the right to lose stability and expand without destabilizing the pulse on the left. After $t = 8000$ sec, when the TW phase velocity had decreased and the pulse width had expanded, the applied temperature difference was reduced, causing the left-hand pulse to decay. The Rayleigh-number gradient was then removed and the Rayleigh number was subsequently adjusted in the range 1.292–1.295 so as to limit the spatial growth or shrinkage of the remaining unstable pulse.

The drifting, destabilized pulse in Fig. 3 is actually strongly unstable and quite difficult to control. After time $t = 15\,000$ sec in the run of Fig. 3, frequent manual adjustments of the Rayleigh number in the range 1.292–1.295 were required to prevent the pulse from either expanding to fill the system or contracting back into a stable, narrow pulse. In order to maintain these structures in a steady state, it has been necessary to use the active servo control described in Sec. III above. Figure 4 shows the performance of an early version of this pulse-width control. The top graph shows the space-time trajectories of the leading and trailing edges of the pulse and the bottom graph shows the Rayleigh number applied by the servo in response to the measured amplitude profile. The tendency of this servo to ring that was mentioned in Sec. III is obvious in the growing oscillations in Rayleigh number. In the run of Fig. 4, the servo parameters had not yet been adjusted to minimize this ringing. Interestingly, it is the trailing edge of the pulse profile which responds strongly to the oscillations in the Rayleigh number.

It has been possible to adjust the parameters of the pulse-width servo program to substantially reduce its ringing from the level shown in Fig. 4. This has been more successful at shorter pulse widths than at longer ones. The standard deviation of the servo-controlled pulse-width variations increases monotonically with width, quadrupling as w increases from 10 to 30, and this is largely due to increased ringing for $w \gtrsim 17$. The square symbols in Fig. 5 show the dependence of the neutral Rayleigh number $r_o(w)$ on pulse width. In order to reduce data scatter due to the ringing of the servo, data points with excessive values of dw/dt and d^2w/dt^2 have been removed from this graph. The solid curve running through these data points is a fit to the form $r_o(w) = r_\infty + r_w w^{-\alpha}$. A least-squares optimization yielded best-fit coefficients $r_\infty = 1.288\,43$, $r_w = 1.050$, and $\alpha = 1.808$. The rms deviation of the data points from the best-fit curve is $\delta r = 8 \times 10^{-4}$, still substantially larger

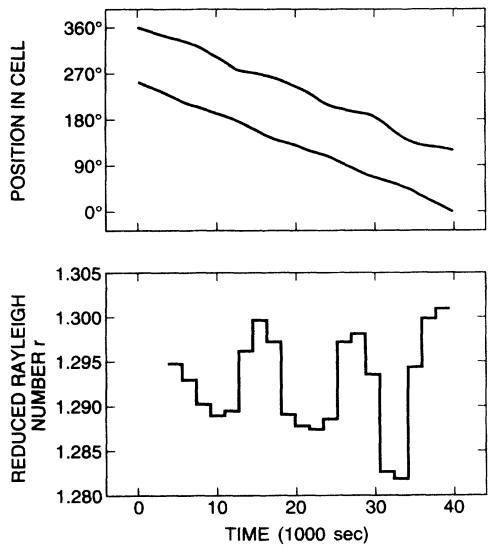

FIG. 4. Behavior of a misadjusted pulse-width servo control. The top graph shows the trajectories of the leading and trailing edges of the pulse amplitude profile, as computed by real-time demodulation of the shadowgraph signal. The underlying TW's travel *downward* in this representation; i.e., the top curve represents the trailing edge and the bottom curve represents the leading edge. The bottom graph shows the Rayleigh number as controlled by the servo program in response to the pulse width measured in the top graph. The servo has been incorrectly adjusted, so that the Rayleigh-number signal exhibits slow, growing oscillations. The velocity of trailing edge of the pulse oscillates in response. The sensitivity of the leading edge of the pulse to the Rayleigh-number oscillations is much weaker.

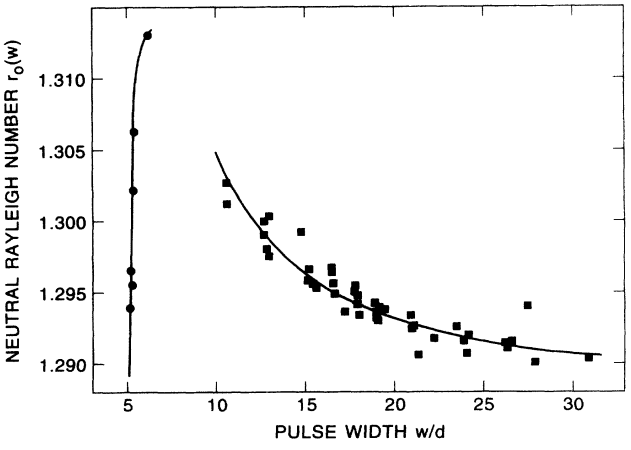

FIG. 5. The neutral Rayleigh number $r_0(w)$ is plotted for stable and unstable pulses at $\psi=-0.127$. The square symbols are the results of servo control of isolated, unstable, wide pulses. The curve through these symbols is a power-law fit using the form given in the text. The solid circles are conventional measurements of the widths of stable, narrow pulses at various Rayleigh numbers, using multiple pulses for fluctuation suppression. These narrow pulses grow unstable above $r_1=1.3132(6)$. No data have been obtained for pulse widths between $w=6$ and 10; in that range, single pulses are destroyed by convectively amplified TW fluctuations.

than the spatial Rayleigh-number nonuniformity. The reader may perceive some vertical bands of points in the scatter of the data about the fitted curve. This structure is an artifact due to residual ringing in the servo control, which causes the Rayleigh number to oscillate while maintaining a reasonably constant width. There is no evidence that $r_0(w)$ is less smooth than the fitted curve. Even with optimized servo control and high spatial uniformity, these confined states are quite difficult to control.

Despite the scatter in the pulse-width-servo data, Fig. 5 clearly shows that the neutral Rayleigh number $r_0(w)$ is a decreasing function of width above $w=11$. Because $dr_0/dw<0$, these confined states are dynamically unstable. This is the fundamental reason for which these "unstable pulses" are so difficult to control. For comparison with this behavior I have plotted as solid circles in Fig. 5 the widths of narrow pulses measured at various Rayleigh numbers. The top point represents the widest such pulse observed in these experiments. The nearly vertical curve which passes through these data points demonstrates that narrow pulses are strongly stable. The language of stability is a natural way to express the insensitivity of the structure of these ubiquitous "stable pulses" to experimental parameters.

Notice that there are no data points in the range $6\lesssim w\lesssim 11$ in Fig. 5. This is not because unstable pulses do not exist in this range, but rather because single pulses in this range of widths are destroyed by TW fluctuations. Attempting to reduce the pulse width from above to below 11 requires increasing the Rayleigh number into a range where such fluctuations no longer have insufficient gain to be seen. The convective amplification and the increased size of the quiescent part of the cell conspire to produce fluctuations strong enough to destroy isolated unstable pulses of widths less than 11. Of course, this could have been prevented by adding a second pulse for fluctuation suppression—this is what was done to obtain the data for the narrow pulses in this figure—but I have chosen only to study isolated unstable pulses in these experiments.

Figure 5 demonstrates one of the most important results of this work. At $\psi=-0.127$, it is possible to create a pulse with any width larger than about 5 times the height of the cell. Wide and narrow pulses are members of the same family of confined states; it is the stability of this state that depends on width. The set of pulse widths is discrete: the equation $r=r_0(w)$ describes a set of measure zero—a curve—in the (r,w) plane. This observation is in accord with the CGLE model discussed in Ref. [6].

The servo control of unstable pulses has been more than adequate to allow steady-state measurements of their spatiotemporal structure for a wide range of widths. These measurements are summarized in Figs. 6–8. The solid circles and full curves in Figs. 6(a) and 6(b) show their drift and phase velocities, respectively. For comparison, the squares and dashed curves repeat the results for stable pulses given in Fig. 1. The unstable-pulse drift velocity is comparable with that of stable pulses, exhibiting a weaker increase with Rayleigh number. The phase

velocity of the TW in the unstable pulses is much slower than that in the stable pulses and it increases rather than decreases with Rayleigh number. I believe that this behavior is unique among all TW states.

Figures 7 and 8 show the demodulated amplitude and wave-number profiles for two ranges of widths. In these and subsequent profiles, a careful method of shifting and averaging was used. At each time step in a data file, spatial demodulation at the measured mean wave number was performed, using very wide spatial bandwidth to avoid distortion. The spatial coordinates at each time step were shifted and scaled so that the 50% points of the trailing and leading edges of the amplitude profile were located at positions 0 and 1, respectively, and the pulse width w for that time step was recorded. The rescaling derived from the amplitude profile was also applied to the wave-number and temporal-frequency profiles. Finally, the shifted and scaled data for all the time steps were binned together in space and averaged, and the abscissas were multiplied by the average width to recover the correct spatial scale. This method allows all measurements of the structure of drifting pulses with slightly varying widths to be shifted together and averaged without distortion.

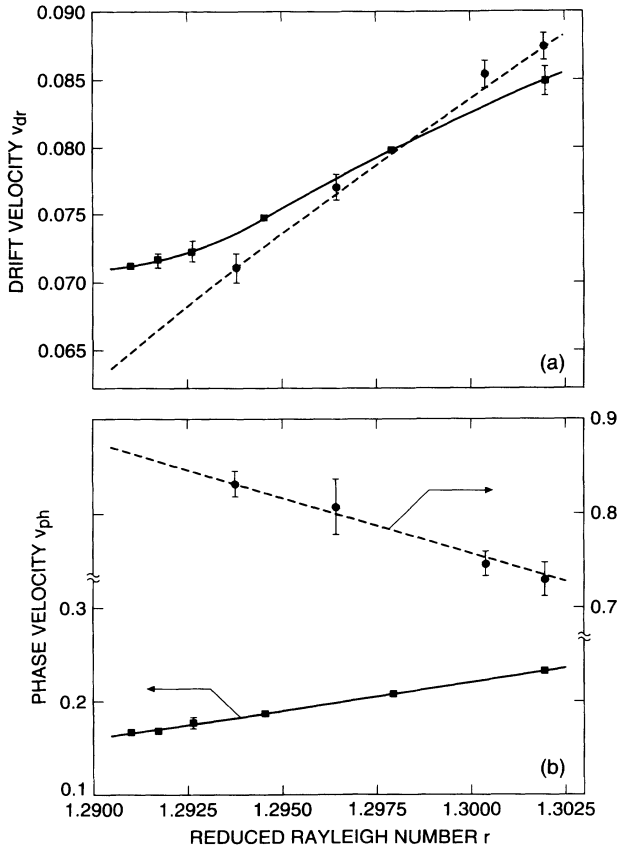

FIG. 6. (a) The drift velocity and (b) TW phase velocity are plotted as functions of reduced Rayleigh number for stable (circles, dashed curves) and unstable (squares, full curves) pulses at $\psi = -0.127$. The unstable-pulse data in these graphs were determined from measurements at servo-controlled pulse widths; the Rayleigh numbers corresponding to these widths were taken from the power-law fit to $r_o(w)$ in Fig. 5. Error bars are shown when larger than the symbol size.

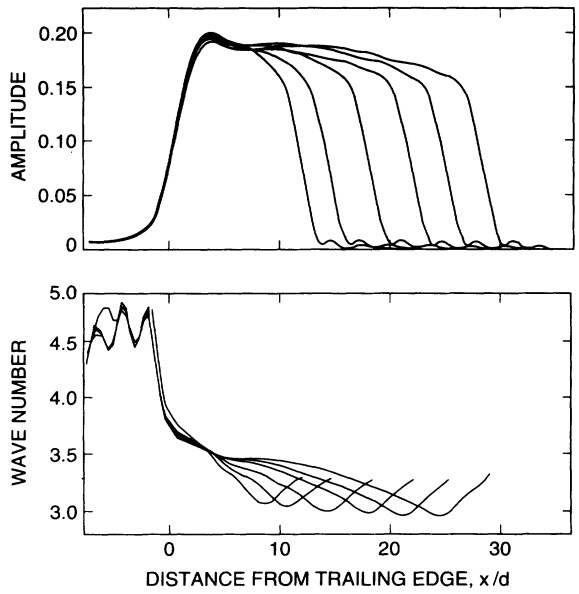

FIG. 7. The top and bottom graphs show the spatial profiles of the amplitude and wave number, respectively, for a series of wide unstable pulses at $\psi = -0.127$. The full width at half maximum (FWHM) pulse widths and average servo-controlled reduced Rayleigh numbers are $w = 11.08(29)$ and $r = 1.3020$, $w = 13.47(21)$ and $r = 1.2980$, $w = 17.21(23)$ and $r = 1.2946$, $w = 21.13(28)$ and $r = 1.2927$, $w = 24.26(29)$ and $r = 1.2917$, and $w = 27.78(31)$ and $r = 1.2910$. In this and subsequent figures showing spatial profiles, the underlying TW's propagate to the right, so that the trailing (upstream) edge is on the left and the leading (downstream) edge is on the right. Note the double minima in the low-amplitude region just ahead of the leading edge in each amplitude profile: these are phase defects.

Figure 7 shows the amplitude and wave-number profiles for steady-state unstable pulses of widths 11 to 28. As detailed in the figure caption, servo control of successively wider pulses was accomplished at decreasing Rayleigh numbers. The structure of the amplitude profiles is identical behind (i.e., to the left of) a point approximately $7d$ downstream from the trailing (i.e., left-hand) edge and the structure in the neighborhood of the leading (i.e., right-hand) edge is also quite similar for all the pulses. With increasing pulse width, the center part of the amplitude profile is simply stretched out to fill the space in between. The five widest pulses in this series also exhibit nearly identical wave-number profiles behind a point approximately $4d$ downstream from the trailing edge; once again, the leading-edge structure is also identical in all pulses and the rest of the profile just interpolates between the two edges. These unstable pulses all exhibit a pair of phase defects just ahead of the leading edge—this is visible as two minima in the low-amplitude regions just ahead of the leading edges of each amplitude profile. The corresponding singularities in the wave-number profiles have been cut out of the graph for clarity. The observation that the spatial structures of confined states

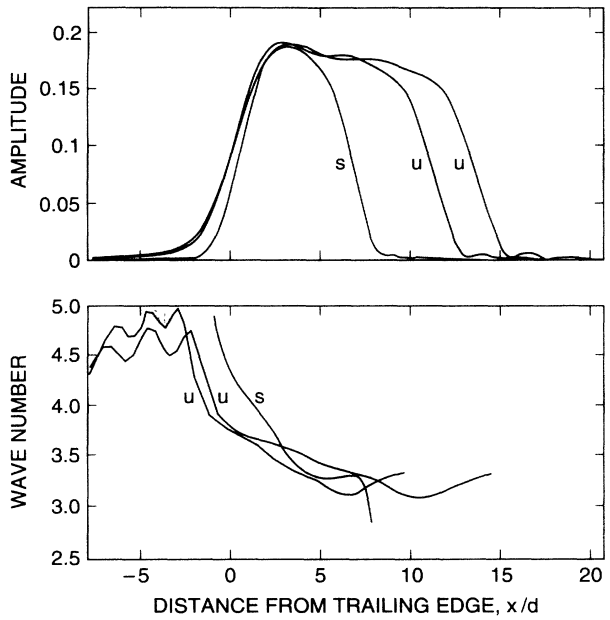

FIG. 8. The top and bottom graphs show the spatial profiles of the amplitude and wave number, respectively, for the two narrowest unstable pulses in Fig. 7 [widths 11.08(29) and 13.47(21)] and for the widest stable pulse observed at $\psi=-0.127$ (width 6.18 FWHM, reduced Rayleigh number 1.312 88). For clarity, the profiles of the narrow pulse have been shifted slightly to the right, and the stable and unstable profiles have been marked *s* and *u*, respectively.

of all widths consist of nominally identical edge structures connected by central regions of varying widths has also been made in the numerical work of Ref. [19].

Figure 8 shows a closer comparison of the two narrowest profiles in Fig. 7 with the structure of the widest stable pulse observed in these experiments. In common with the structure of TW pulses at $\psi=-0.072$ [10], the stable pulse does not exhibit the leading-edge phase defect seen in the unstable pulses; rather its wave number drops at the leading edge and its amplitude profile exhibits a smooth, weak, leading-edge shoulder. The trailing edge of the amplitude profile of the stable pulse also appears sharper than that of the unstable pulses. These microscopic structural differences may reflect the reasons for the differences in the stability of wide and narrow confined states. Broadly speaking, however, all pulses exhibit similar structure: a leading-edge amplitude shoulder and a wave-number profile which decreases sharply at the trailing edge and more gently in the main body of the pulse. The pulse structure changes continuously as the width is increased. This general description applies to all defect-free confined states.

V. STABLE CONFINED STATES $\psi=-0.253$

The results of the preceding section partially answered the first two of the open questions posed in the Introduction: whether both wide and narrow confined states exist at a given separation ratio and what the relationship is between them. Now I turn to the third question: the nature of the locking band and of the lack of drift observed for arbitrary-width confined states at $\psi=-0.25$. In this section, I address the basic issues of drift, locking, and stability for a narrow range of confined-state widths at $\psi=-0.253$, and I present measurements of the structure of wide confined states. A fuller exploration of the stability of confined states over a wide range of widths at other values of ψ is deferred until Secs. VI and VII.

Figure 9 shows the space-time paths of the roll boundaries for a confined state of width 21.059(29) at $\psi=-0.253$. The TW's in this state propagate to the left at velocity $v_{\rm ph}=1.480$, while the amplitude profile drifts in the opposite direction at a much lower velocity $v_{\rm dr}=-0.0237$. Contrary to the observations made in a cell of much worse uniformity in Ref. [2], all confined states observed in this work drift continuously. I have allowed confined states like this one to drift around the cell for weeks, taking approximately 60 h ($4000\tau_v$) for a round-trip. The lack of drift observed in Ref. [2] was apparently an experimental artifact.

Quantitative measurements of the drift and the spatial growth of wide confined states are presented in Figs. 10 and 11. To produce each data point in these graphs, a confined state was allowed to equilibrate for several hours at constant Rayleigh number and then a series of flow-visualization images was recorded over the next several hours. I did not wait for spatial expansion or shrinkage to disappear; rather, one point of these experiments is to test the applicability of Eq. (1) for arbitrary expansion velocity. The leading- and trailing-edge positions were determined from demodulated TW amplitude profiles, and differentiating in time yielded the front velocities v_l and v_t and the expansion velocity Δv. The dependence of these three velocities on Rayleigh number is shown in Fig. 10. It is difficult to identify clear trends with Rayleigh number in the trailing- and leading-edge velocities

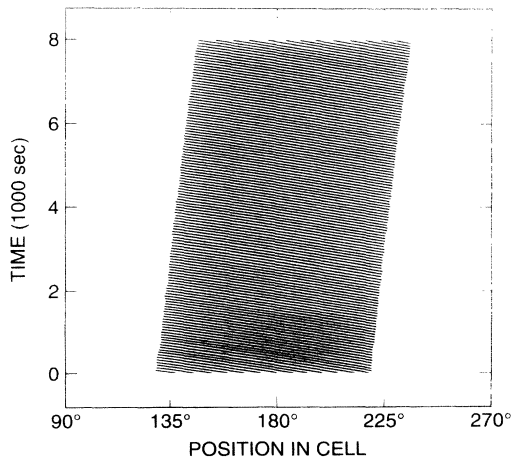

FIG. 9. This space-time plot shows the drift of a wide confined state at $\psi=-0.253$. The width of this state was servo controlled at 21.059(29) to match that of one of the unstable pulses in Fig. 7. The average Rayleigh number during this run was $r=1.3402$.

plotted in Figs. 10(a) and 10(b), and their difference, the drift velocity, also exhibits scatter; see Fig. 11(a). This scatter is associated with the nonzero expansion velocity in most of these data; see Fig. 10(c). Eliminating this effect by servo controlling the confined-state width has allowed a more precise measurement of the drift velocity. This is presented for $\psi=-0.210$ and -0.167 in Secs. VI and VII.

The confined-state expansion velocity plotted in Fig. 10(c) increases with Rayleigh number, with a slope of about 3. The data exhibit substantial scatter; a fit to a cubic polynomial in r matches the data only to within $\delta\Delta v=0.0033$ rms. It might be thought at first that the slight flattening of the trend of the data seen in the range $1.335 \lesssim r \lesssim 1.340$ represents a locking band obscured by the scatter. However, both of these features are caused in fact not by locking but by the dependence of the expansion of the confined state on its width. As described above in Sec. III, I extracted this dependence by fitting the data points $\Delta v(r,w)$ to the sum of a cubic in r and a linear function $\beta(w-\bar{w})$, where $\bar{w}=10$ is the average experimental width. Using the fit parameter β, the width dependence of $\Delta v(r,w)$ can be removed by computing $\Delta\bar{v}(r)=\Delta v(r,w)-\beta(w-\bar{w})$ for each data point. This width-corrected expansion velocity is plotted vs Rayleigh number in Fig. 11(b). The error bars in this graph are somewhat larger than those in Fig. 10(c) because the confined-state width w is not constant in time during most of the measurements; this introduces uncertainly in the width correction $\beta(w-\bar{w})$. Nonetheless, the width correction has reduced the scatter in the data to 0.0015 rms and has revealed a smooth dependence of $\Delta\bar{v}$ on r. The fitted function of r passes through the horizontal axis with slope $\tau_o^{-1}=3.27(20)$ at an intercept $r_v=1.336\,48(23)$. r_v is the unique value at which a confined state of width $\bar{w}$ neither grows nor shrinks. To within this very high precision, there is no locking band.

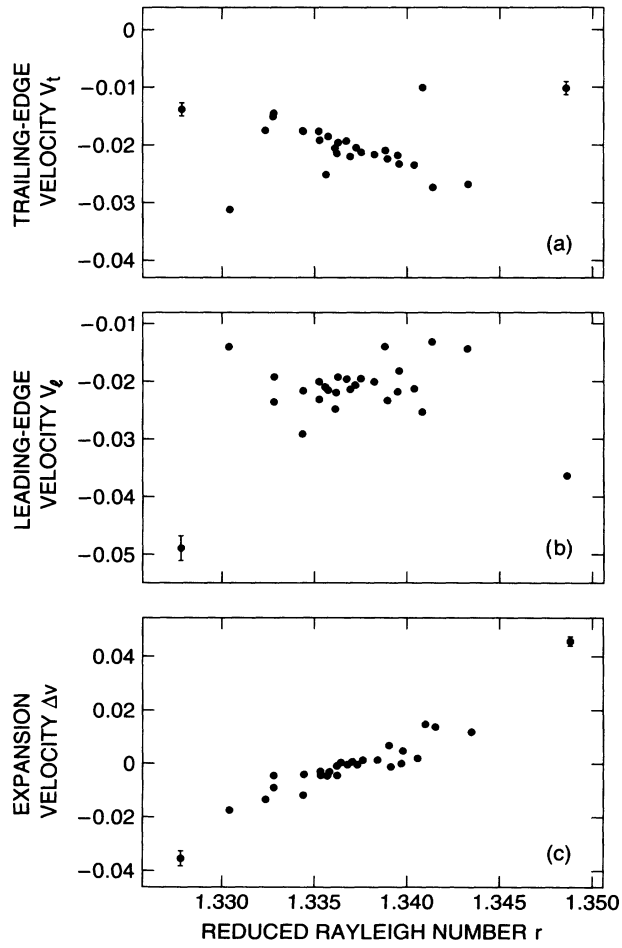

FIG. 10. (a) The trailing-edge, (b) leading-edge, and (c) expansion velocities are plotted as functions of reduced Rayleigh number for confined states at $\psi=-0.253$. Error bars are shown when larger than the symbol size.

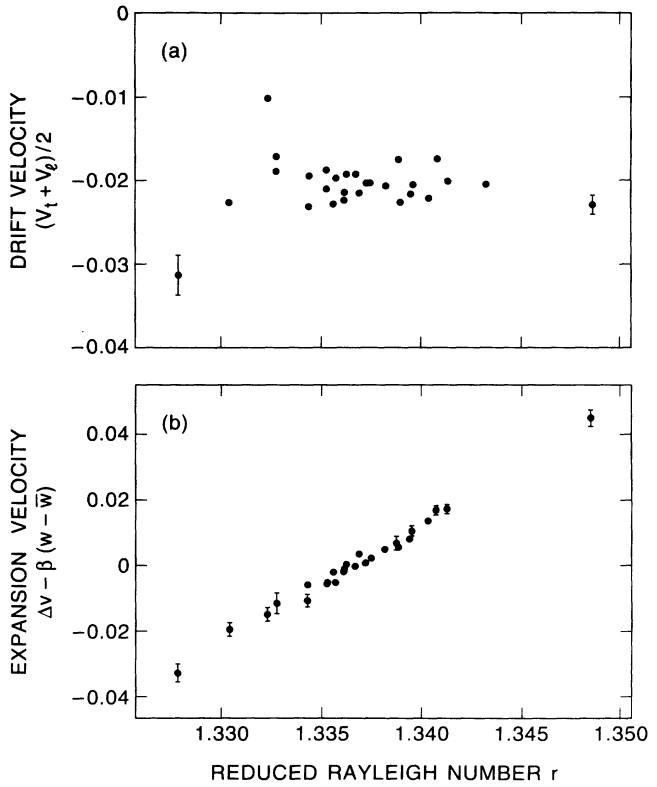

FIG. 11. (a) The drift velocity and (b) the width-corrected expansion velocity for the data of Fig. 10 are plotted as functions of the Rayleigh number. The average drift velocity is $-0.0205(34)$. The width correction has revealed the expansion velocity at $\bar{w}=10$ to be a smooth function of Rayleigh number, with no "locking band." A single data point w width $w=25.5$ has been excluded from this graph; see the text and Fig. 12.

As in the previous discussion of confined states at $\psi=-0.127$, it is useful to recast these results in terms of stability. Figure 12 shows a graph of the neutral Rayleigh number $r_o(w)=r-\tau_o\Delta v$ as a function of w. The fit in the preceding paragraph corresponds to fitting the data for $w<20$ with a straight line; the fitted slope is $dr_o/dw=4.8(3)\times10^{-4}$. Because of the apparent break

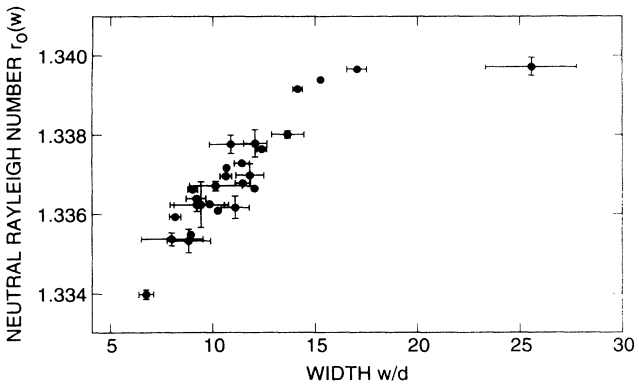

FIG. 12. The neutral Rayleigh number $r_o(w)$ is plotted as a function of pulse width for the $\psi=-0.253$ data of Figs. 10 and 11. Below the break in slope at $w\sim 17$, these data are well fit by a straight line of slope $4.8(3)\times 10^{-4}$. The behavior of the neutral Rayleigh number for $w\gtrsim 17$ is documented in more detail in subsequent experiments at $\psi=-0.210$ and -0.167. In comparing these results with those in Fig. 5, note that there are no measurements here for pulses of width $w\lesssim 7$.

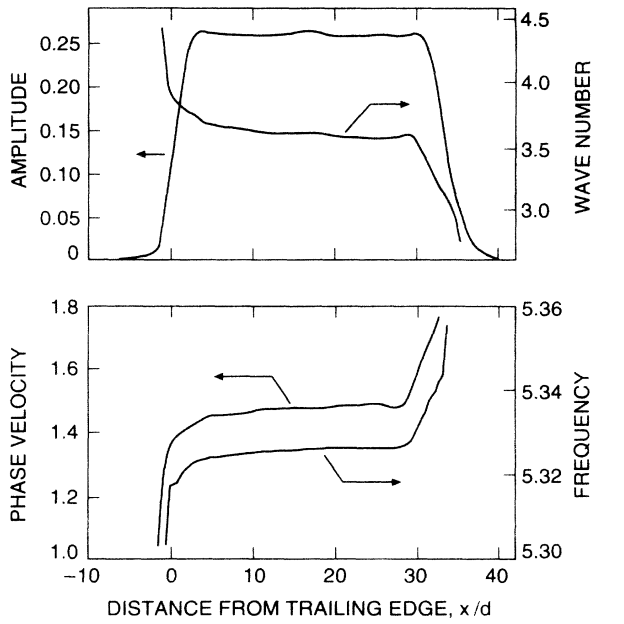

FIG. 13. Spatiotemporal structure of a confined state of width 32.72(7) at $\psi=-0.253$. The Rayleigh number is 1.340 57. The top graph shows the amplitude and wave-number profiles. The bottom graph shows the demodulated temporal-frequency profile and the phase-velocity profile; the latter is the ratio of the former and the wave-number profile.

in the slope of $r_o(w)$ near $w=17$, the single point at $w=25.5$ was not used in the fit. Because $dr_o/dw>0$, confined states with $w\lesssim 17$ are dynamically stable. Qualitative observations of much wider confined states suggest that dr_o/dw remains weakly positive out to at least $w=33$. The stability of confined states with $w\gtrsim 7$ seen at this separation ratio stands in contrast to the unstable confined states seen for the same range of widths in Fig. 5.

Figure 13 documents the spatiotemporal structure of a very wide, stable confined state at $\psi=-0.253$: this state had time-independent width $w=32.72(7)$. The amplitude and wave-number profiles shown in the top graph in this figure are by now quite familiar; in particular, the characteristic rapid decreases in wave number at the leading and trailing edges, accompanied by a much gentler decrease in the main body of the pulse, are characteristic [20]. The bottom graph of Fig. 13 shows the spatial structure of the oscillation frequency and the TW phase velocity. The oscillation frequency is remarkably uniform in the main body of the confined state.

Figure 14 shows a comparison between the stable, $\psi=-0.253$ confined state of Fig. 9 and an unstable pulse of the same width ($w=21.1$) produced at $\psi=-0.127$. The amplitude profile of the unstable pulse at $\psi=-0.127$ has been multiplied by a scale factor to match the height of its companion (Fig. 21 below shows the behavior of the amplitude of confined states of width 21.1 as a function of ψ). Aside from this difference in magnitude, the principal difference between these amplitude profiles lies in the structure of the leading edge: the stable confined state lacks the amplitude nulls seen in the leading edge of the unstable pulse. The wave-number gradient is seen to be greater in the main body of the unstable pulse than that in the stable confined state. Once again, the stable structure exhibits a sharp drop in its wave number at the leading edge, with no sign of the phase defects seen in the leading edge of the unstable pulse.

The main results of this section are that wide confined states at $\psi=-0.253$ drift continuously, are stable, exhibit a spatiotemporal structure that fits into the trends noted

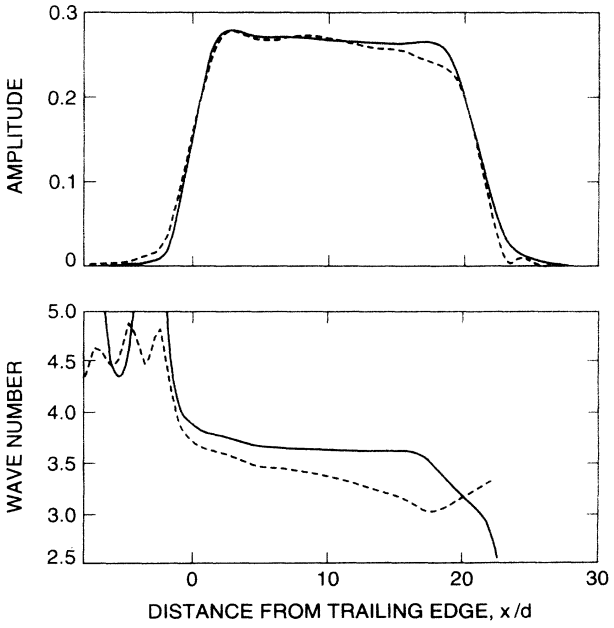

FIG. 14. Comparison of the structures of a stable confined state at $\psi=-0.253$ [solid curves; width 21.059(29)] with an unstable state of the same width at $\psi=-0.127$ [dashed curves; width 21.13(28)].

at $\psi=-0.127$, and do not exhibit the previously observed locking band.

VI. STABLE CONFINED STATES $\psi=-0.210$

The experiments described in the preceding section explored the spatial growth and stability of stable confined states in a rather narrow range of widths. The analysis showed that a minor modification of Eqs. (1) and (2) accurately modeled the very slightly nonlinear Rayleigh-number dependence of the expansion velocity Δv over a wide range of Δv. The experiments presented in this section are meant to be complementary: their purpose is to measure the width dependences of the characteristic time $\tau_o(w)$ and the neutral Rayleigh number $r_o(w)$ over a wide range of w, with less attention paid to producing and explaining large expansion velocities.

The experiments at $\psi=-0.210$ began with measurements of the expansion velocity Δv as a function of Rayleigh number and confined-state width, as in Fig. 10. These measurements covered widths in the range $7\lesssim w\lesssim 27$. The initial analysis of these data proceeded as described in Sec. III: I parametrized the width dependence of τ_o as $\tau_o=\tau_{oo}+\beta_\tau w$, where τ_{oo} and β are adjustable parameters. For each measurement of $\Delta v(r,w)$, I computed the expansion-corrected neutral Rayleigh number $r_o=r-\tau_o\Delta v$ as previously, eliminating a few points for which Δv was so large that w exhibited excessive uncertainty. These data for $r_o(w)$ were then fit to a heavily smoothed cubic spline function of w and the fit parameters τ_{oo} and β_τ were adjusted to minimize the fit error.

The data points in Fig. 15 show the expansion-corrected neutral Rayleigh number plotted vs w, and the curve is the smoothed spline fit. The degree of smoothing in this procedure is somewhat arbitrary, but it is easy to detect when the smoothing is too strong (the curve becomes too straight and χ^2 grows too large) or too weak (the curve develops wiggles which decrease χ^2 but are undoubtedly unphysical). Averaging the results obtained for several different degrees of smoothing gave $\tau_{oo}=0.317(5)$ and $\beta_\tau=-0.0050(3)$. The rms deviation of the data from the curve in Fig. 15 is $\delta r_o=5.6\times10^{-4}$, somewhat larger than the average error bar. The slope of the curve in the range $10\lesssim w\lesssim 15$ is $dr_o/dw=2.7\times10^{-4}$, about half of that found for $\psi=-0.253$.

The principal qualitative result here is that τ_o depends on w. It may be possible to reduce the rms error of the fit in Fig. 15 by trying a different functional form for this dependence or by introducing more adjustable parameters, but the lowest-order linear dependence assumed above has been adequate to demonstrate that this width dependence does exist. This is made clear in Fig. 16, where I plot Δv as a function of Rayleigh number for subsets of the data for which w is near the two selected values $\bar{w}=7.0$ and $\bar{w}=23.1$. In order to reduce the scatter in the graph caused by the spread of widths in each subset, the Rayleigh number has been corrected for width by writing $\bar{r}=r-r_o(w)+r_o(\bar{w})$ for each data point. The straight lines in Fig. 16 represent the fitted function $\Delta v(\bar{r})=[r-r_o(\bar{w})]/\tau_o(\bar{w})$. These lines clearly match the data and exhibit noticeably different slopes, confirming the width dependence of $\tau_o(w)$.

Figure 17 shows another way to assess the adequacy of this fit procedure: the scaled expansion velocity $\tau_o(w)\Delta v$ is plotted against the Rayleigh-number difference $r-r_o(w)$ for all data points in Fig. 15. A linear fit to these scaled data has a slope 0.978(26), consistent with the expected value 1.0, confirming the correctness of Eq. (1) in explaining these data. The rms deviation of the scaled data from this linear fit is $\delta r=3.2\times10^{-4}$, compa-

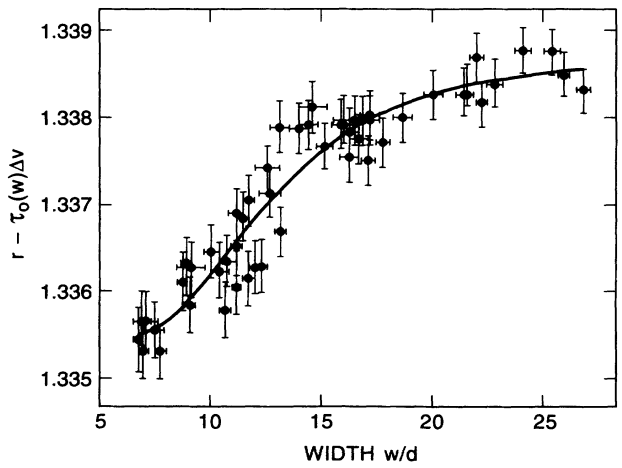

FIG. 15. The symbols represent data for the neutral Rayleigh number $r_o(w)$, corrected for the nonzero expansion velocity Δv using a width-dependent characteristic time $\tau_o(w)$. The curve is a smoothed cubic spline fit to these data points. The width dependence of τ_o has been adjusted to minimize the error in the spline fit. $\psi=-0.210$.

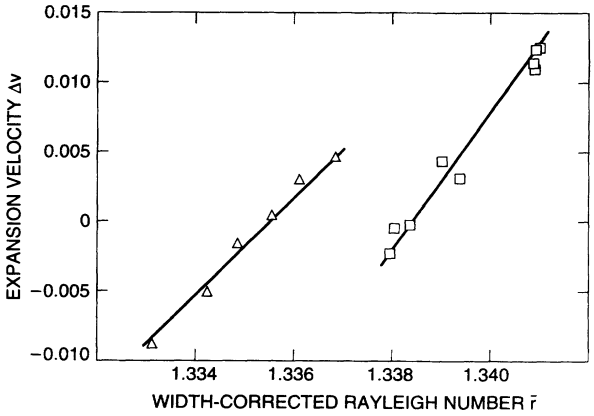

FIG. 16. The confined-state expansion velocity is plotted as a function of reduced Rayleigh number for two subsets of the data at $\psi=-0.210$. Triangles, average confined-state width $\bar{w}=7.0(0.4)$; squares, $\bar{w}=23.1(2.0)$. Error bars are smaller than the size of the symbols. To correct for slight differences between the actual widths w and the average widths $\bar{w}$, the Rayleigh number r for each data point has been changed to $\bar{r}=r-r_o(w)+r_o(\bar{w})$. The straight lines represent the two-parameter spline fit to entire data set. The different slopes for the two subsets plotted here illustrate the substantial dependence of the characteristic time τ_o on w.

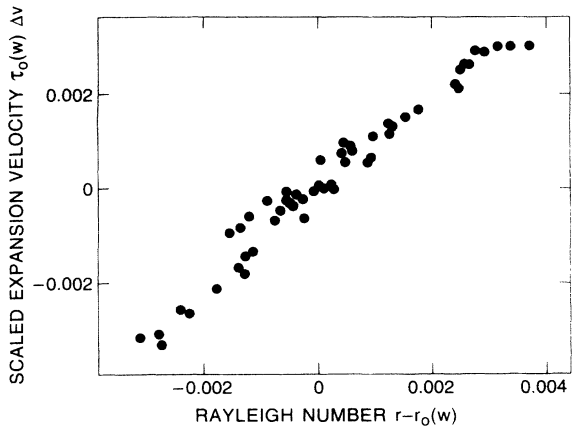

FIG. 17. The scaled expansion velocity $\tau_o(w)\Delta v$ is plotted against the Rayleigh-number difference $r-r_o(w)$ for the data of Fig. 15. The two-parameter spline fit in Fig. 15 corresponds to fitting these data with a straight line of slope 1.

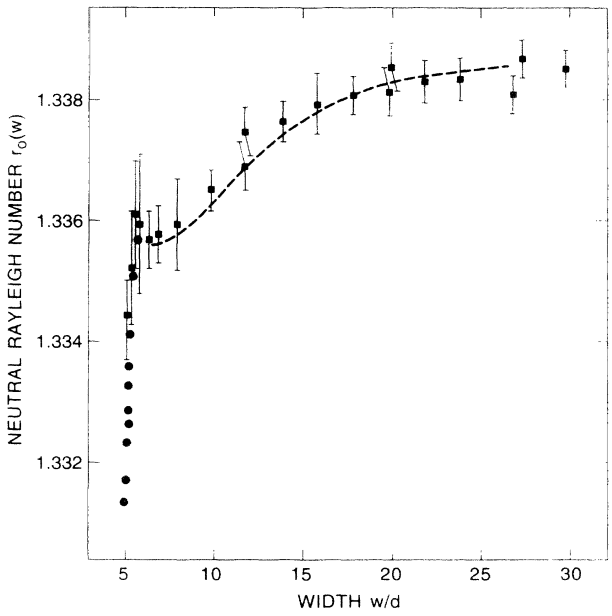

FIG. 18. The square symbols represent direct measurements of the neutral Rayleigh number $r_o(w)$ using servo control of stable, wide confined states at $\psi=-0.210$. The dashed curve is the spline fit derived from the non-servo-controlled data in Fig. 15. The solid circles represent measurements of the width of narrow pulses made at fixed Rayleigh number without servo control. For clarity, the errors bars have been deleted from these data, and a few points which would fall below the bottom of the graph have been eliminated.

rable to the random uncertainties in the raw data. A better parametrization of $\tau_o(w)$ would probably not reduce this error by very much.

Since the quantitative interpretation of the results presented so far depends on an assumed width dependence for τ_o, I have augmented these data with a series of direct measurements of $r_o(w)$ using the width-control servo described in Sec. III above. Recall that the result of this procedure is a series of measurements of $\Delta v(r,w)$ from which I calculate $r_o(w)=r-\tau_o(w)\Delta v$. Under servo control, the expansion velocity Δv is kept so small that uncertainties in $\tau_o(w)$ are irrelevant. It is worth noting in this context that servo control of *stable* confined states exhibited no ringing or "inertia" as was seen with unstable pulses at $\psi=-0.127$. Servo control of stable confined states is not necessary for their characterization; it is just a convenience which allows direct measurement of $r_o(w)$. For stable confined states, Eq. (1) is a quantitatively accurate description of confined-state expansion and stability.

The square symbols in Fig. 18 show the servo results for $r_o(w)$ at $\psi=-0.210$, while the dashed curve represents the spline fit in Fig. 15. This curve clearly lies inside the error bars, but the data would be even better described by a curve which is slightly higher than the spline fit for $w\lesssim 15$ and slightly flatter for $w\gtrsim 20$.

Note that the error bars for the servo data at the lowest widths in Fig. 18, $5\lesssim w\lesssim 8$, are quite large in comparison with those at large w. Stable confined states become quite difficult to control in this regime, and this seems to be because their width does not quite match that of a branch of slightly narrower, strongly stable pulses. Uncontrolled measurements of the width of the latter pulses are shown as solid circles in Fig. 18. The observation of this new branch of stable, narrow pulses at $\psi=-0.210$ contains the rest of the answer to the first two questions posed in the Introduction: a full range of confined-state widths seems to be possible at least for all ψ in the range $-0.210\le\psi\le-0.127$. The lower Rayleigh-number limit of the existence of narrow pulses is measured to be $r_2=1.3265(9)$ at $\psi=-0.210$.

The spatiotemporal structure of narrow pulses at $\psi=-0.210$ is similar to that observed for $\psi\gtrsim-0.13$. The spatial profile of the TW amplitude exhibits the same leading-edge shoulder, and the wave-number profile exhibits the same strong gradient. Figures 19(a) and 19(b) show the pulse width w and drift velocity v_{dr}, plotted in the usual way as functions of Rayleigh number. The variation of pulse width with Rayleigh number is somewhat stronger than at less negative ψ, and the range of existence is somewhat reduced. These comparisons will be made more explicit in Sec. IX below. The drift velocity v_{dr} increases rapidly with Rayleigh number, as at smaller $|\psi|$. v_{dr} also exhibits a slight dependence on expansion velocity, which was not strictly zero for several of these non-servo-controlled measurements. To reduce the resulting scatter in the data in Fig. 19(b), I have plotted a corrected drift velocity $\bar{v}_{dr}=v_{dr}-0.795\Delta v$. The $(r-r_0)^{1/2}$ dependence seen in previous experiments does not fit these data as well as at less negative ψ, although a pronounced downward curvature would still be seen in any fitted curve.

Measurements of the drift velocity of confined states over a wide range of widths at $\psi=-0.210$ are gathered together and plotted as a function of width in Fig. 20. The rapid variation of v_{dr} for narrow pulses stands in strong contrast to the much slower variation observed for

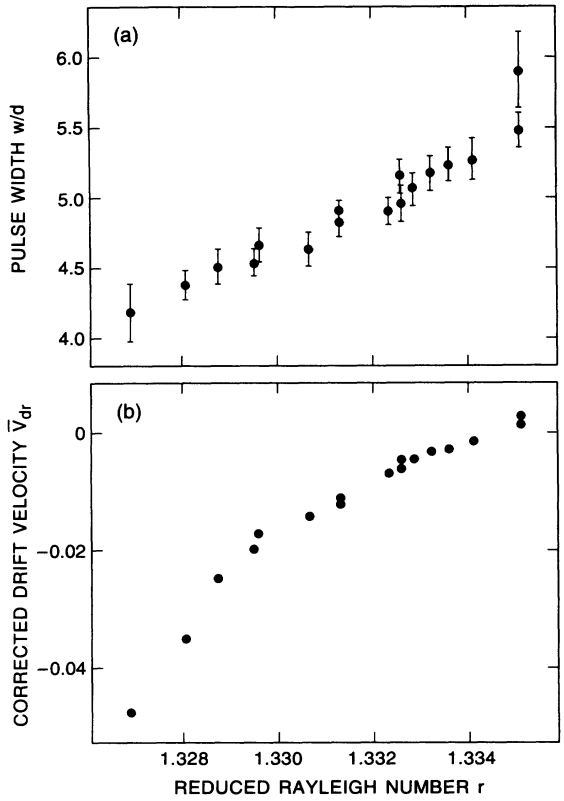

FIG. 19. (a) The width of narrow pulses observed at $\psi=-0.210$ is plotted as a function of reduced Rayleigh number r. The width increases approximately linearly with r until a width of about 6 has been reached. At this width, pulses become less stable, as evidenced by the jump in width here and by the corresponding change in slope in Fig. 18. (b) The pulse drift velocity is plotted as a function of r. As explained in the text, a small correction has been made for the nonzero expansion velocity observed in some of the data. Error bars in (b) are smaller than the symbol size.

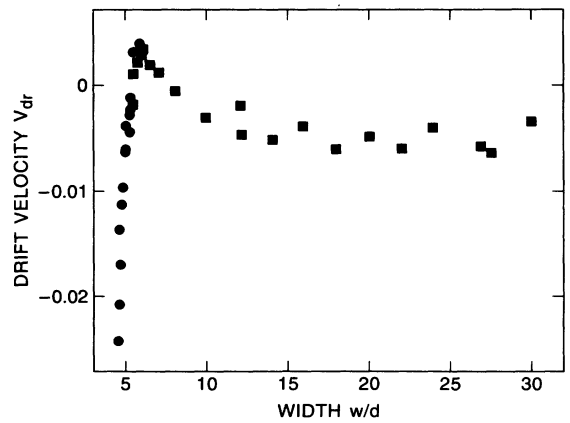

FIG. 20. Drift velocity vs width for stable confined states at $\psi=-0.210$. As in previous figures, square symbols represent measurements on servo-controlled confined states, while circles pertain to uncontrolled narrow pulses. The drift velocity increases rapidly with width for narrow confined states and then decreases slowly at higher widths. Error bars are smaller than the symbol size.

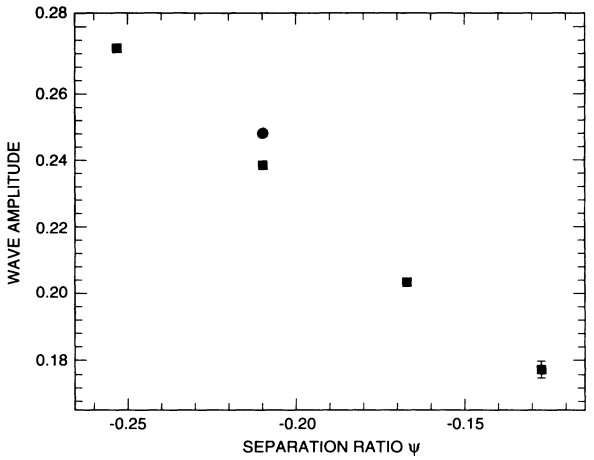

FIG. 21. The spatially averaged TW amplitude $\int A(x)dx/w$ is plotted vs separation ratio for confined states of width $w=21.08\pm0.11$. The square symbols are derived from the amplitude profiles $A(x)$ measured during servo control of the confined-state width. The circular data point is derived from a non-servo-controlled data set which was subjected to slightly different numerical processing. The difference between it and the corresponding square data point at $\psi=-0.210$ is an indication of the reproducibility of these measurements.

servo-controlled wide confined states. Interestingly, the dependence in Fig. 20 is nonmonotonic. This is also the case for unstable pulses at $\psi=-0.127$; see Fig. 33 below. Note that wide confined states drift much more slowly at this separation ratio than at $\psi=-0.253$; compare with Fig. 11(a). This comparison will also be made more explicit in Sec. IX below.

The TW amplitude and wave-number profiles of wide, stable confined states at $\psi=-0.210$ are quite similar to those shown in Figs. 13 and 14 for $\psi=-0.253$. Indeed, except for a vertical scale factor, width-matched amplitude profiles for stable confined states at all $\psi\lesssim-0.167$ are virtually identical. The spatially averaged TW amplitude for confined states of width 21.1 is shown as a function of separation ratio in Fig. 21. A smooth dependence on ψ is observed. The amplitude of the unstable pulse at $\psi=-0.127$ happens to match this trend, even though Fig. 14 showed systematic differences between the profiles of stable and unstable confined states of this width. The wave-number profiles of stable confined states at $w=21.1$ at different ψ do not match as exactly as those of the TW amplitude. However, the variation with ψ is quite weak and will not be detailed further here.

VII. STABLE CONFINED STATES $\psi=-0.167$

The measurements presented in the preceding section were repeated in a series of experiments at $\psi=-0.167$. The analysis and its results were similar to those presented in the preceding section, so this description will be brief. As at $\psi=-0.210$, both stable, wide confined states and strongly stable narrow pulses are observed. Figure 22 shows the width and drift velocity of narrow pulses as

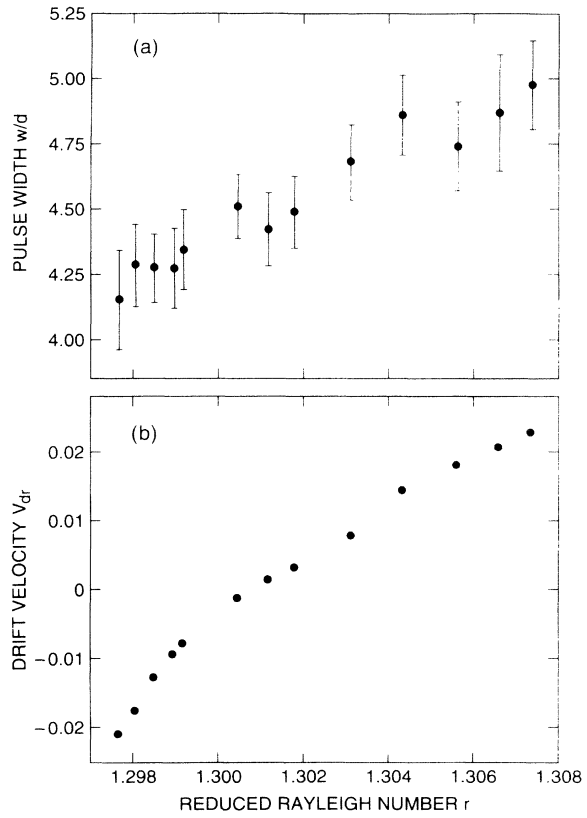

FIG. 22. (a) The width and (b) drift velocity of narrow pulses at $\psi = -0.167$ are plotted as functions of the reduced Rayleigh number r. The increasing trends in both these numbers are similar to those seen for $\psi = -0.210$ in Fig. 19.

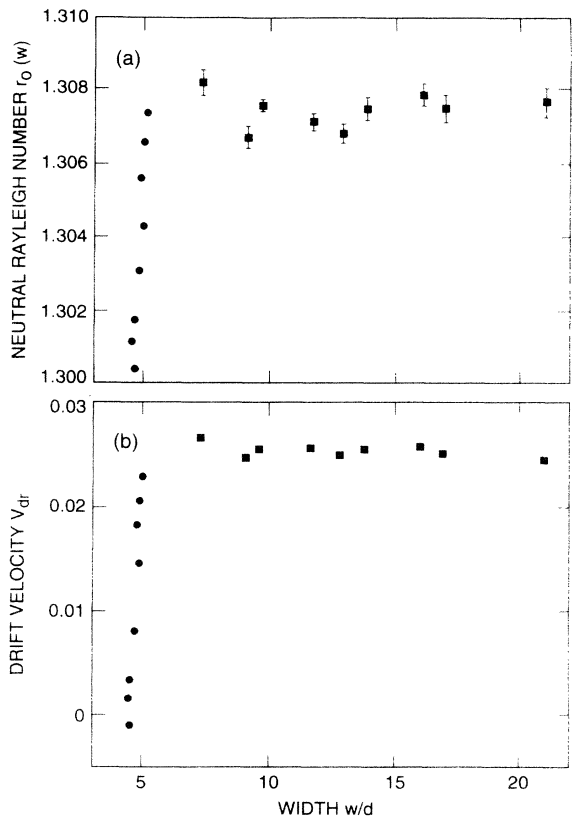

FIG. 23. (a) The neutral Rayleigh number $r_o(w)$ and (b) the drift velocity v_{dr} are plotted as functions of width w for confined states at $\psi = -0.167$. As in previous figures, squares are derived from runs in which the confined-state width was servo controlled, while circular symbols represent uncontrolled measurements. For $w \gtrsim 7$, both r_o and v_{dr} are essentially independent of w.

functions of Rayleigh number r. Once again, the pulse width varies approximately linearly with r, and the drift velocity varies strongly with r, exhibiting a clear downward curvature that does not quite match the square-root dependence seen at $\psi \geq -0.127$. The limits of stability of narrow pulses at $\psi = -0.167$ are found to be $r_2 = 1.2975(6)$ and $r_1 = 1.3080(10)$.

Servo-controlled observations of wide confined states were also made at this separation ratio. The results of these experiments are shown in Fig. 23. Both $r_o(w)$ and v_{dr} are essentially independent of confined-state width for $w \gtrsim 7$. There was enough of a variation of the expansion velocities Δv in this series of experiments that I could extract estimates for the characteristic time $\tau_o(w)$ from linear fits of Δv vs r for widths in the range $7 \gtrsim w \gtrsim 17$. I found $\tau_o = 0.373(21)$, independent of w over this range of widths.

No results were obtained in this series of experiments for confined states with widths greater than $w = 21$. This is because wide, servo-controlled confined states tend to develop spatiotemporal defects when the servo program makes changes in the Rayleigh number. Indeed, the data point for $w = 21$ in Fig. 23 lost stability in this way after only about 8 h under servo control. Wide confined states at this separation ratio seem to be much more susceptible to the formation of defects than those at the other separation ratios studied. However, this susceptibility does not imply that wide, undefected confined states cannot be created at $\psi = -0.167$. By making very gentle, manual changes in the Rayleigh number, I have made wide, undefected confined states with slightly nonzero Δv. Persistent confined states which exhibit repeated spatiotemporal defects are described in the next section.

VIII. NEW CONFINED STATES

The experimental section of this paper began in Sec. IV with a discussion of the "intrinsic destabilization" process by which narrow, stable pulses lose stability at $\psi = -0.127$. This process was documented in Fig. 3 above, where a strong Rayleigh-number gradient and a transient fluctuation-absorbing pulse were used to create an isolated unstable pulse. However, a wide, drifting, confined state is not the only outcome of such an experiment; indeed this was already illustrated in Fig. 2. There, two narrow pulses were allowed to expand above stability threshold r_1, and in that case, their trailing edges remained approximately stationary, while their leading edges expanded in space at the velocity of the underlying slow TW.

What confined structure would have resulted in the experiment of Fig. 2 if one of the pulses had been removed and the expansion of the other had been stopped before the cell filled with TW's? The answer is presented in Fig. 24. In analogy with Fig. 3 above, the goal of this experiment was to produce an isolated confined state in a uniform system. The run in Fig. 24 began with two narrow pulses in a strong Rayleigh-number gradient, as in Fig. 3. When the Rayleigh-number profile was made uniform again at time $t=9660$ sec, the destabilized pulse looked very much like the corresponding structure in Fig. 3. In this run, however, the pulse expansion took place in the manner illustrated in Fig. 2, with a nearly motionless trailing edge and a leading edge advancing at the speed of the underlying TW. The result, at the end of time period represented in Fig. 24, was a confined state of nearly motionless rolls in a uniform system. It is worth pointing out that a run of this type at $\psi=-0.072$ was already described in Fig. 21 of Ref. [10]. In that experiment, however, the system also contained other TW pulses, and these interacted with the confined state of nearly steady rolls.

I have repeated this kind of experiment several times and found this state impossible to control. The nominally motionless rolls have a strong tendency to suddenly start moving, sometimes reversing directions repeatedly, and the width of the state is unstable. In the run of Fig. 24, for example, the state continued to expand slowly, nearly filling the experimental cell. An attempt to stabilize this expansion by reducing the Rayleigh number from 1.300 17 to 1.288 26 at time 61 845 sec was ineffective, while a further reduction to 1.284 29 at time 79 450 sec caused the confined state to collapse rapidly. This is shown in Fig. 25. In the present case, I was able to arrest this collapse in time to form a wide, unstable pulse of the type discussed above. Usually, however, the unchecked collapse ends in the production of a narrow, stable pulse. The possibility of creating *stable* confined states of motionless rolls at small separation ratio is considered in Sec. IX below.

I end the data-presentation part of this paper with a description of another qualitatively new convective structure: a weakly unstable, defected confined state. The discovery of this state came about because of a difference in the evolution of narrow pulses at $\psi=-0.127$ and

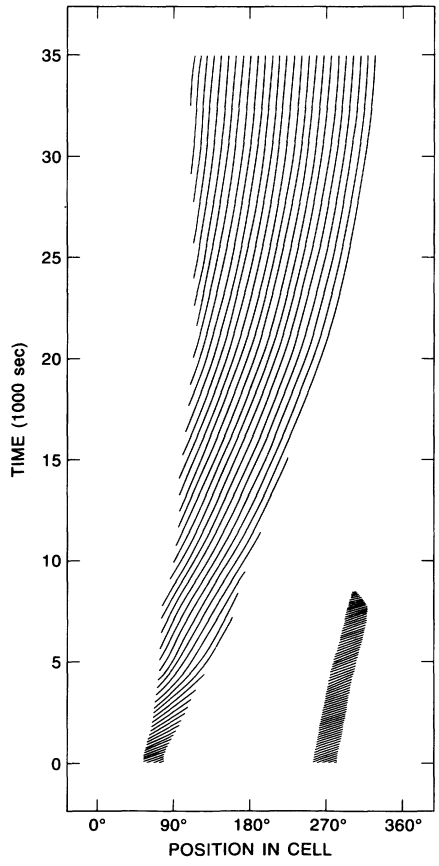

FIG. 24. This space-time plot shows the production of a wide, unstable state of nearly motionless convective rolls, in analogy with the experiment illustrated by Fig. 3. At the beginning of this run, a strong Rayleigh-number gradient caused the pulse on the left to expand, while the weak pulse on the right remained narrow and absorbed TW fluctuations. At time $t=9660$ sec, after the weak pulse disappeared, spatially uniform heating was restored, at Rayleigh number $r=1.306\,78$. This was reduced to $r=1.300\,17$ at time $t=13\,090$ sec. At this Rayleigh number, the destabilized pulse evolved into a very slowly expanding state of nearly motionless rolls.

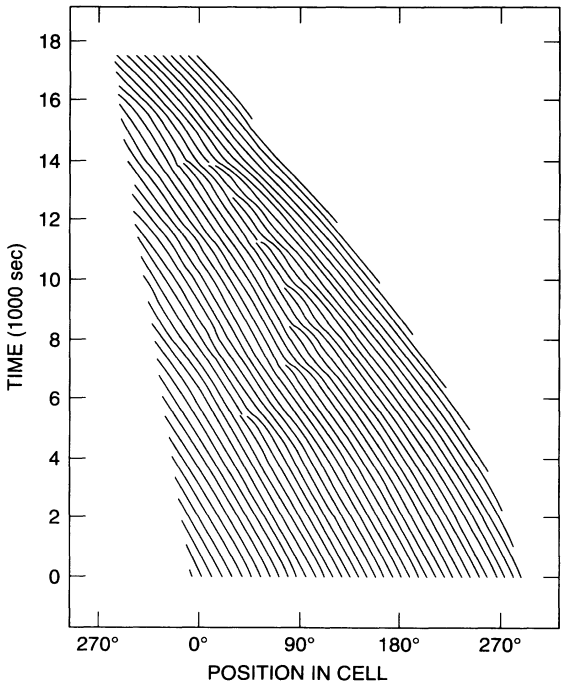

FIG. 25. Collapse of the confined state produced in Fig. 24. Time $t=0$ in this figure corresponds to time $t=77\,700$ sec in Fig. 24. 15 855 sec before the beginning of the time period in the present figure, r was reduced to 1.288 26 in an attempt to arrest the expansion of the state in Fig. 24. At time $t=1750$ sec in the present figure, r was reduced again to 1.284 29. This precipitated the collapse of the confined state. Note the roll-pair annihilation events which accompany this collapse.

$\psi \leq -0.210$. The usual way I produce isolated, narrow pulses, as documented in previous publications [10,13,16], is to launch a small-amplitude, localized disturbance which decomposes into two oppositely propagating wave packets; see Fig. 1 in either article of Ref. [13] for an illustration of this initiation process. Local heating is applied to the vicinity of one of these wave packets so that its amplitude grows much more strongly than that of the others. As the wave packet grows, linear dispersion causes its spatial width to increase substantially. When the amplitude of the selected wave packet is so large that nonlinear effects become evident, the Rayleigh number is reduced. This causes the other, weaker wave packets to decay and the stronger wave packet to shrink into a narrow, nonlinear pulse. The spatial growth and subsequent narrowing can be seen at the bottom of Fig. 3 above.

It is this intermediate phase of spatial narrowing that differs substantially at different values of ψ. For $\psi \leq -0.167$, a narrow wave packet splits off the leading edge of the pulse, travels ahead into the region of decreased Rayleigh number, and decays. The narrow structure it leaves behind quickly settles into the shape of a pulse. This evolution is not very sensitive to the Rayleigh number; it is very easy to make narrow pulses at $\psi \leq -0.167$ this way. For $\psi = -0.127$, however, this intermediate phase is much less reproducible. If the Rayleigh number is kept too high for too long during this phase, then the wave packet does not simply shrink into a narrow pulse. Instead, the TW's at the leading edge grow in amplitude, their phase velocity decreases relative to those upstream at the trailing edge, and spatiotemporal defects form in between. This is a *defected confined state.* At $\psi = -0.127$, persistent, wide, defected confined states are easily made and have been studied in great detail. At $\psi = -0.167$, it is also possible to make persistent defected confined states. They tend to form not during the intermediate phase of spatial narrowing of nonlinear wave packets, as at $\psi = -0.127$, but rather when an attempt is made to make an undefected confined state grow to $w \gtrsim 19$ by increasing the Rayleigh number. At $\psi \leq -0.210$, defects are never seen in confined states, except as transients.

Figure 26 shows examples of defected confined states at three different Rayleigh numbers at $\psi = -0.127$. It can be seen in this figure that the expansion velocity of these confined states increases with Rayleigh number; this observation is made quantitative below. The narrow defected confined state in Fig. 26(b), whose expansion velocity is close to zero, consists of three regions of TW's with different phase velocities separated by two lines of roll-pair annihilations or spatiotemporal dislocations. The TW phase velocity is approximately constant in each of these three regions, and the velocity decreases as one moves downstream from one region to the next. The defect lines separating the three regions are located at distances 4 and 10 (in units of the cell height) downstream from the trailing edge. Interestingly, the formation of defects in the line closer to the trailing edge is periodic in time, with period $7.76(9)\tau_v$. The expanding and contracting confined states shown in Figs. 26(a) and 26(c) exhibit

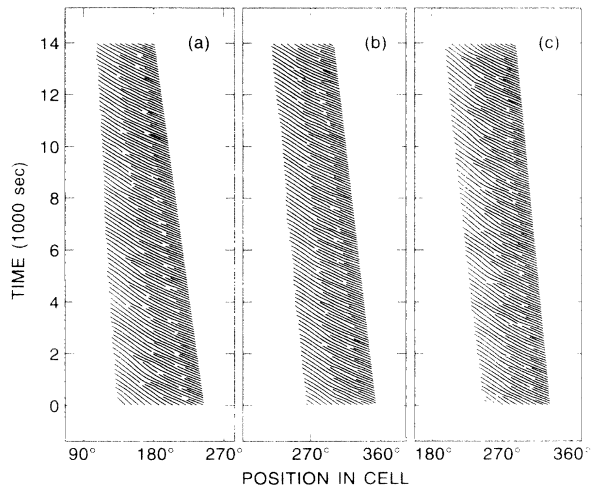

FIG. 26. Space-time diagrams show the behavior of narrow defected confined states at $\psi = -0.127$ at slightly different Rayleigh numbers: (a) $r = 1.275\,47$, (b) $r = 1.280\,44$, and (c) $r = 1.284\,89$. The middle diagram shows a confined state of nearly constant width in which roll-pair annihilations occur periodically in time at a position $4d$ downstream from the trailing edge.

the same qualitative features, albeit with less regularity in the timing and locations of the spatiotemporal defects.

As shown in Fig. 27, it is also possible to make very wide defected confined states. Once again, the expansion velocity increases with increasing Rayleigh number, and the confined state in Fig. 27(b) has nearly constant width. The TW's at the leading edge of these very wide confined states exhibit a noticeably lower phase velocity than those upstream, and the spatiotemporal defects which separate them from the fast TW's are arrayed much more irregularly in space time.

The leading-edge and trailing-edge velocities have been measured for defected confined states over a wide range of Rayleigh numbers and widths. Both velocities are observed to exhibit an approximately bilinear dependence on width and Rayleigh number. I define the notation for fits to this dependence as follows:

$$v_x = v_{0x} + \alpha_x (r - r_v) + \beta_x (w - \bar{w}) , \tag{4}$$

where the subscript x is l for the leading edge, t for the trailing edge, and Δv for the expansion velocity, which was separately computed as the time derivative of the confined-state width. Here $\bar{w} = 38$ is the mean width for all the data and $r_v = 1.282\,16$ is the Rayleigh number at which a confined state of width $\bar{w}$ exhibits zero expansion velocity. Applied to the expansion velocity Δv, Eq. (4) is equivalent to Eq. (1) assuming a linear dependence for $r_o(w)$; the coefficient $\alpha_{\Delta v}$ is equivalent to the inverse of the characteristic time τ_o. The first three lines in Table II contain the results of linear least-squares fits to this form for v_l, v_t, and Δv. The fit to the data for Δv was performed separately but is of course not independent of the other two fits. Notice that $\beta_{\Delta v}$ is positive. Defected

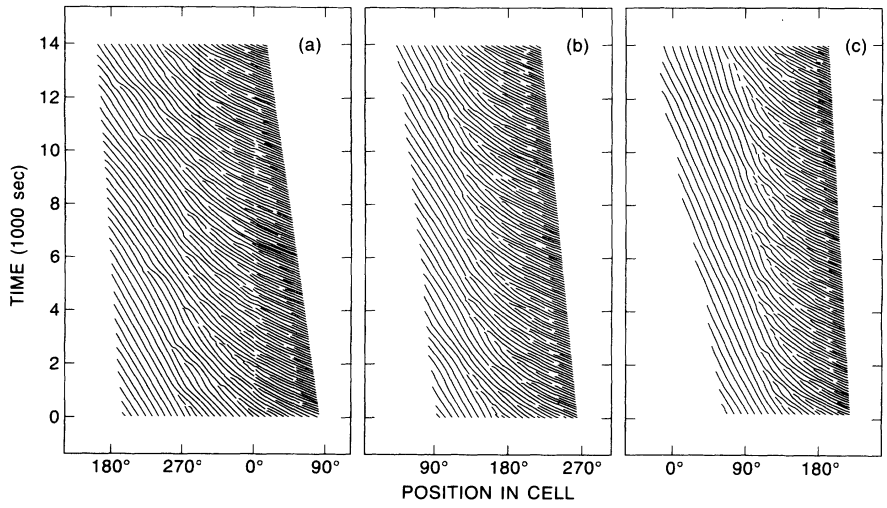

FIG. 27. Space-time diagrams of very wide defected confined states at Rayleigh numbers $r=1.275\,23$ (a), $1.281\,94$ (b), and $1.291\,16$ (c). The TW phase velocity at the leading edge of such wide confined states is extremely low.

confined states are thus unstable at this separation ratio, but weakly so, as detailed in Sec. IX below.

Figure 28 shows the Rayleigh-number dependence of the front and expansion velocities corrected for width by subtracting off the $(w-\bar{w})$ term computed in the fits. The leading-edge velocity shown in Fig. 28(a) increases with Rayleigh number with almost the same square-root dependence seen for the drift velocity of stable pulses at this value of ψ. In contrast, the trailing-edge velocity decreases with r [Fig. 28(b)], so that the drift velocity is only weakly dependent on Rayleigh number: the total variation of drift velocity is less than $\pm 10\%$ for all the data. The expansion velocity [Fig. 28(c)] increases with Rayleigh number with slope $\alpha_{\Delta v}=4.10$.

The phase velocity $v_{\rm ph}^{f}$ of the fast TW's at the trailing edge of the defected confined states can be accurately measured, and its dependence on width is shown in Fig. 29(b). A bilinear fit to the form of Eq. (4) has been applied to these data—see Table II—but the fit coefficients are so small that a weighted average of these data is the best characterization of their behavior: $v_{\rm ph}^{f}=0.903(15)$. This is to be computed with the phase velocity 2.4967 measured for linear TW's at this separation ratio. The phase velocity $v_{\rm ph}^{s}$ measured at the leading edge of these confined states is much less well defined. As shown in Table II, the dependence of this velocity on width and Rayleigh number is not negligible. Figure 29(a) shows the width dependence, corrected for Rayleigh number by subtracting off the fitted $(r-r_v)$ term. Very long defected confined states have very slow TW's at their leading edges.

TABLE II. Coefficients of bilinear fits to velocities measured in defected confined states.

Data	v_0	α	β	rms error
v_l	0.042 40	+2.27	$+2.36\times10^{-4}$	0.0025
v_t	0.042 16	−1.93	-0.42×10^{-4}	0.0017
Δv	$\equiv 0$	+4.10	$+2.59\times10^{-4}$	0.0033
$v_{\rm ph}^{s}$	0.809 8	−16.9	−0.0116	0.039
$v_{\rm ph}^{f}$	0.893 3	−1.63	-1.6×10^{-4}	0.01

Characterizing the structure of defected confined states is more difficult than in the case of the steady confined states discussed above, because this structure is not unique or constant. But there are some repeatable

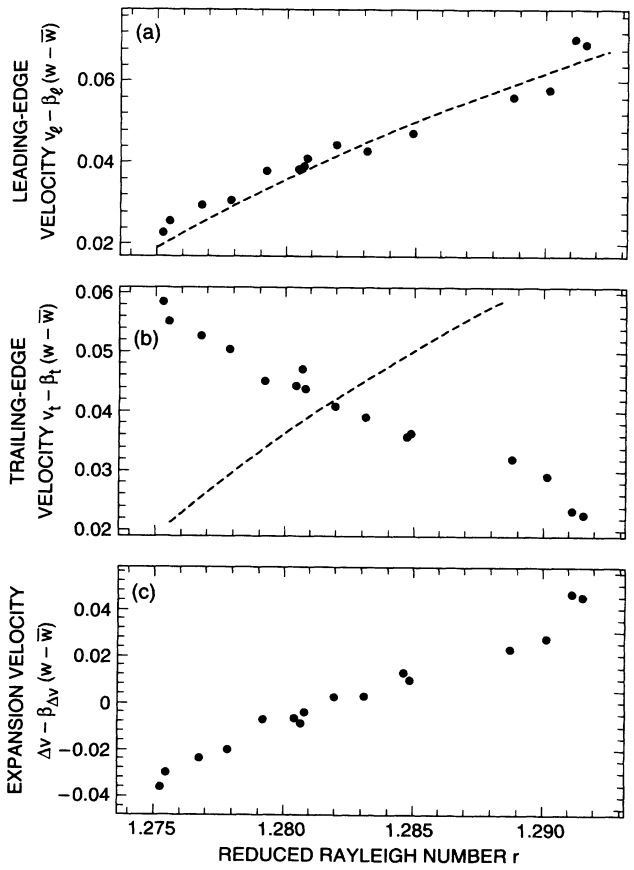

FIG. 28. Rayleigh-number dependence of the (a) leading-edge, (b) trailing-edge, and (c) expansion velocities for defected confined states at $\psi=-0.127$. Error bars are smaller than the symbol size. The fitted width dependence has been subtracted in each case. The dashed curves in (a) and (b) both represent the drift velocity of narrow pulses at this separation ratio, copied from Fig. 1(a).

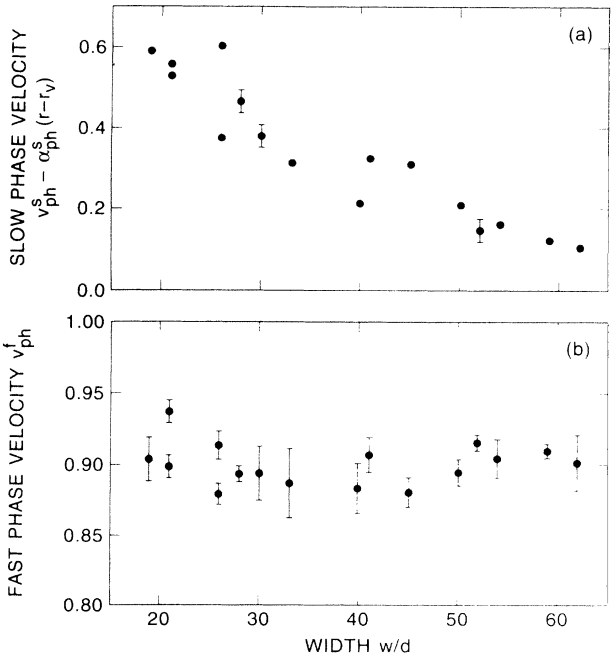

FIG. 29. (a) The Rayleigh-number-corrected phase velocity of the slow TW at the leading edges of defected confined states at $\psi = -0.127$ is plotted as a function of confined-state width. A strong decrease with width is evident. (b) The phase velocity of the fast TW at the trailing edges of defect confined states is plotted as a function of width. There is no width or Rayleigh-number dependence stronger than the error bars.

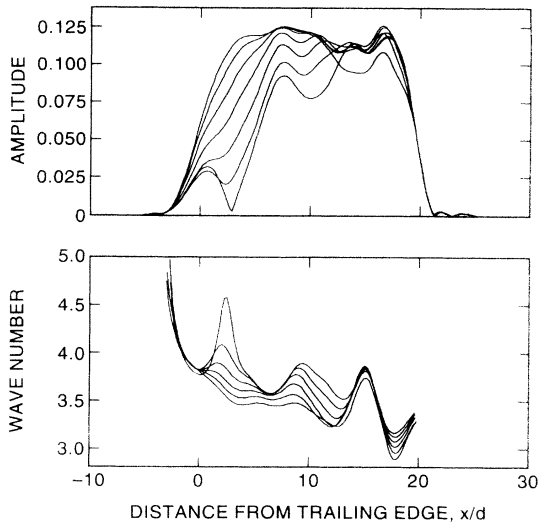

FIG. 30. A temporal sequence of amplitude (top) and wave-number (bottom) profiles is shown for the defected confined state of Fig. 26(b). The widest amplitude profile and the lowest wave-number profile correspond to the first time step in this sequence, and the time step is $0.666\tau_v$, compared with the regular time delay $7.76(9)\tau_v$ between successive defects. For clarity, the strongly peaked wave-number profile at the seventh time step is not shown.

features to be observed, as seen in Figs. 30 and 31. Figure 30 shows amplitude and wave-number profiles made at a sequence of times during the run of Fig. 26(b). This confined state exhibited nearly zero expansion velocity, and the first defect downstream from the trailing edge appeared periodically in time, so that a few samples of the data during one defect cycle are enough to fully characterize the structure. The seven time steps in the amplitude-profile graph in the top of Fig. 30 start with the widest profile; as time proceeds, the trailing edge moves forward and down, resulting in a cusp-shaped defect at the last time step. During this period of time, the leading edge is hardly affected. In subsequent time steps, the trailing edge grows back up again. The same time period begins with the lowest wave-number profile in the bottom graph of Fig. 30. As time proceeds, the local wave number increases throughout the main body of the confined state, culminating in a singular peak at the location of the defect (for clarity, the sharply peaked profile corresponding to the last time step in the amplitude-profile graph has been deleted from the wave-number graph in Fig. 30).

Figure 31 shows the amplitude and wave-number profiles exhibited at one instant by a very wide defected confined state. These profiles were made very close to a time at which two phase defects were present. Note that the wave-number profile exhibits very large wiggles downstream of the first defect, while wave-number modulations are almost absent downstream of the second defect. This leads to the impression that the TW's produced by the first defect suffer some kind of convective modulational instability as they travel downstream; the growth of this instability culminates in the second phase defect.

As noted above, defected confined states are also seen at $\psi = -0.167$. I have examined these states only enough

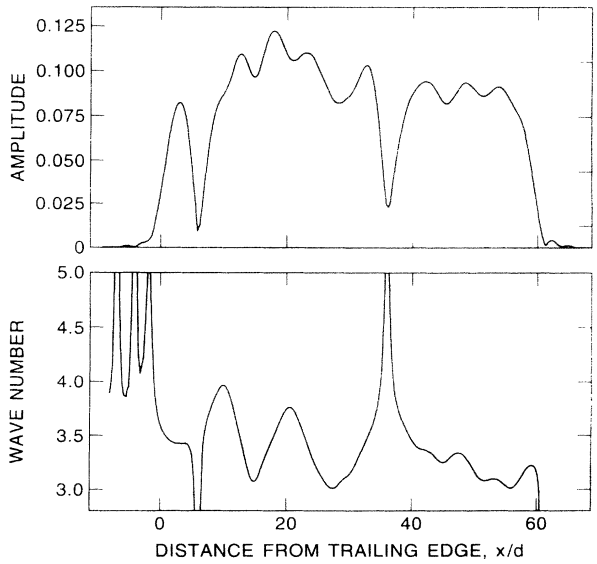

FIG. 31. Amplitude and wave-number profiles exhibited at one instant by a very wide defected confined state at Rayleigh number $r = 1.279\,20$. Two phase defects are present; strongly modulated TW's exist in the spatial region between them.

to verify that this qualitative behavior is the same as $\psi=-0.127$. I have made a single quantitative measurement: at $r=1.306\,75$, a defected confined state of width 33.28(20) drifted at $v_{dr}=-0.026\,89(7)$, expanded with $\Delta v=0.002\,94(14)$, and created defects accurately periodically in time, with period $5.902(25)\tau_v$.

IX. DISCUSSION

The main goal of the experiments described in this paper has been to construct a unified experimental picture of defect-free confined states of TW convection. This picture has turned out to be rather simple: there is a discrete set of such states. This set includes confined states with all widths greater than about 5 times the cell height. Their properties vary continuously with experimental parameters. In particular, confined states of all widths drift at a constant velocity which vanishes only for a measure-zero set of parameters. A secondary goal of this work has been to search for qualitatively new confined states. Two such states have been found; one of these, the defected confined state, has been characterized in detail at $\psi=-0.127$.

In the analysis of the data presented in this paper, it has been convenient to regard the confined-state width w and the separation ratio ψ as the two independent parameters needed to describe confined-state behavior. In this language, Eq. (1) has been proposed as a model of the dynamics and stability of confined states. This model has been found to be quantitatively accurate for wide confined states at $\psi\leq-0.167$ and for defected confined states at $\psi=-0.127$. For the unstable pulses seen at $\psi=-0.127$, a second-time-derivative term appears necessary.

The stability and range of existence of confined states can be described in terms of the neutral Rayleigh number $r_o(w)$. The measurements of this quantity of all confined states at $\psi=-0.127$, -0.167, and -0.210 are plotted together in Fig. 32. This graph shows explicitly that narrow pulses ($w\lesssim 6$) are very strongly stable at $\psi=-0.127$ and less strongly stable at more negative ψ. The domain of existence of narrow pulses decreases strongly as ψ is made more negative than -0.127. Wide confined states are very weakly stable for $\psi\leq-0.210$ and strongly unstable at $\psi=-0.127$. At $\psi=-0.167$, confined states with $w\gtrsim 7$ are approximately *neutrally stable:* $r_o(w)$ is nearly independent of w. Defected confined states at $\psi=-0.127$ (dotted line in Fig. 32) are very weakly unstable.

The shape of the function $r_o(w)$ determines the stability of confined states but not the time scale of their dynamics. This information is contained in the characteristic time $\tau_o(w)$. The analysis of the data for $\psi=-0.210$ revealed that $\tau_o(w)$ is smaller for very wide, defect-free confined states than for narrow ones. However, the linear decrease of $\tau_o(w)$ with width that was assumed in that analysis may not be accurate. This is suggested by the observation that $\tau_o(w)$ is independent of width for $7\lesssim w\lesssim 17$ at $\psi=-0.167$. I have not thought it important to clarify this quantitative detail. My qualitative observation is that τ_o is very short for narrow pulses, although this has not been explicitly measured.

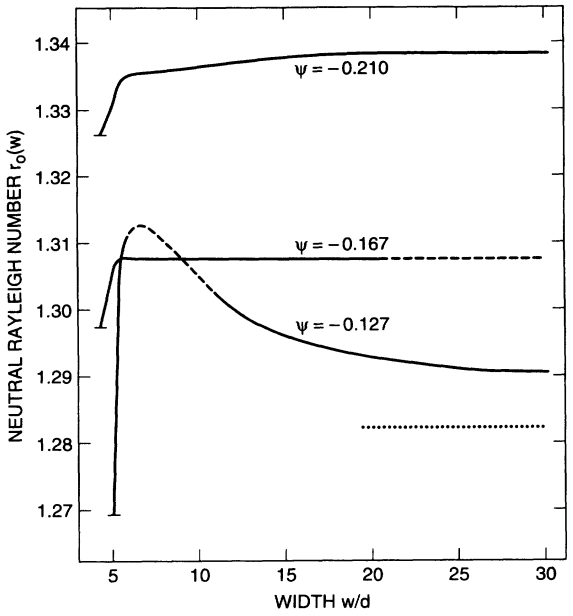

FIG. 32. The neutral Rayleigh number $r_o(w)$ is plotted as a function of width for defect-free confined states at $\psi=-0.127$, -0.167, and -0.210 (solid curves) and for defected confined states at $\psi=-0.127$ (dotted curve). The result for $\psi=-0.253$ shown previously in Fig. 12 overlaps the curve for $\psi=-0.210$ and has therefore been deleted for clarity. The horizontal bars at the left ends of the solid curves denote the lower limits r_2 of existence of narrow pulses. As indicated by the dashed segments, the solid curve for $\psi=-0.127$ has been interpolated in the range $6\lesssim w\lesssim 11$, and the curve for $\psi=-0.167$ has been extrapolated beyond $w=21$.

Table III shows the separation-ratio dependence of τ_o for different confined states. For defect-free confined states, this evaluation was explicitly done for $w=12$ where possible. τ_o is seen to decrease to a very low value as ψ is increased from -0.253 to -0.127. This is one reason why unstable pulses at $\psi=-0.127$ evolve so rapidly that they require active control. More relevant for this experimental control is the product $\gamma=-\tau_o^{-1}dr_o/dw$; this is the linear growth rate of perturbations to steady-state solutions of Eq. (1). As shown in

TABLE III. Dynamics of wide confined states. *S*1 is a stable confined state; dr_o/dw is evaluated for width $w=12$. *S*2 is a stable confined state; both $\tau_o(w)$ and dr_o/dw are evaluated for width $w=12$. *U* is an unstable confined state; dr_o/dw is evaluated for width $w=12$. *D* is a defected confined state; no width dependence has been measured. Parentheses denote uncertainties.

ψ	State	τ_o	$-\tau_o^{-1}dr_o/dw$
−0.253	*S*1	0.306(19)	−0.001 57(14)
−0.210	*S*2	0.257(6)	−0.001 05(10)
−0.167	*S*2	0.373(21)	−0.000 10(10)
−0.127	*U*	0.08(2)	+0.022(4)
−0.127	*D*	0.244(6)	+0.000 26(2)

Table III, γ is negative for $\psi \leq -0.167$; these weakly stable confined states evolve slowly. γ is strongly positive for $\psi = -0.127$; unstable pulses evolve rapidly. I suspect that the growth rate of the unstable pulse at $\psi = -0.072$ that was shown in Fig. 20 of Ref. [10] was even more strongly positive. Defected confined states at $\psi = -0.127$ are also unstable, but so weakly that they do not require active control.

Confined states of all widths drift continuously through the experimental cell. Figure 33 brings together with measurements of the drift velocity of defect-free confined states made in this work, plotted vs width w. Consistent with previous measurements at $-0.123 \leq \psi \leq -0.072$ [10], v_{dr} varies strongly with Rayleigh number and separation ratio for narrow pulses. The drift velocity of wide confined states also varies with parameters. At $\psi = -0.127$, v_{dr} decreases rapidly with width for $w \lesssim 20$. This dependence is less pronounced at $\psi = -0.210$ and absent at $\psi = -0.167$. The rather uncertain measurements at $\psi = -0.253$, represented by the shaded rectangle, are roughly consistent with the trend of the more accurate data at less negative ψ.

The results in Fig. 33 make it clear why previous experiments in slightly nonuniform cells produced motionless, wide confined states which exhibited a locking band [2]. The reason for this behavior is somewhat different from the reason that the first observations of narrow pulses in an annular cell found them to be motionless [9,10,12,13]. The drift velocity of narrow pulses varies quite strongly with Rayleigh number. Thus, in a nonuniform cell, a pulse drifts towards the nearest location in the cell where the Rayleigh number is such that $v_{dr} = 0$ and stops there. If the Rayleigh number is then changed, this location moves, and the pulse follows, coming to rest at the new location. In contrast, the drift velocity of wide pulses for $-0.25 \lesssim \psi \lesssim -0.19$ is very low and nearly independent of Rayleigh number. Because wide confined states drift so slowly, they are easily pinned by local inhomogeneities in the cell. I speculate that pinning takes place at geometric rather than thermal features in the cell; thus changing the Rayleigh number slightly does not change the location or size of the confined state. Because v_{dr} depends so weakly on Rayleigh number, a substantial change in R is required to unpin the confined state. This picture accounts for the motionlessness of wide confined states and for the existence of a locking band in previous experiments. Overcoming these problems in order to observe the drift of wide confined states has required the development of a convection cell which is both thermally and geometrically very uniform.

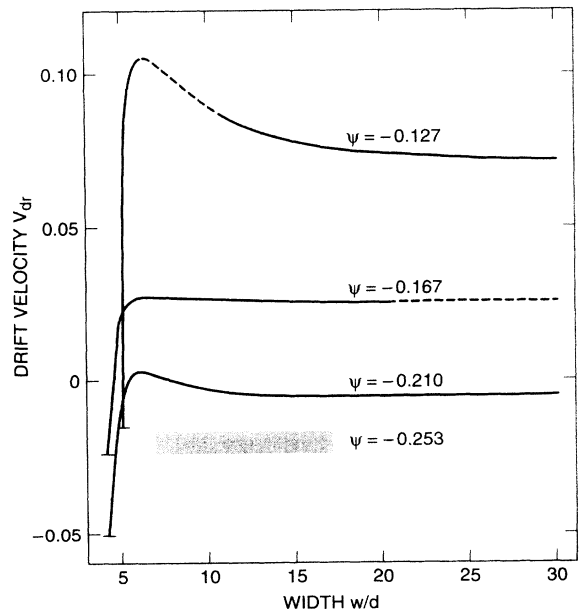

FIG. 33. The solid curves represent the measurements of the width dependence of the drift velocity of defect-free confined states at $\psi = -0.127$, -0.167, and -0.210 which exhibit zero expansion velocity. As in Fig. 32, dashed segments indicate extrapolated and interpolated values. Drift-velocity measurements at $\psi = -0.253$, whose dependence on expansion velocity has not been carefully studied, are represented by the shaded rectangle.

The spatiotemporal structure of narrow pulses has been well documented for $\psi \geq -0.072$ in previous experiments [9–11]. In this paper, I have extended these measurements to wide confined states and to more negative ψ by computing the TW amplitude, wave-number, and frequency profiles. Certain common features are seen for all defect-free confined states. In particular, a strong wave-number gradient is seen near the trailing edge, connecting to a weaker gradient in the main body of the confined state. Unstable confined states exhibit a few features which seem to be generically different from stable confined states; namely, a stronger wave-number gradient in the main body of the pulse and phase defects just ahead of the leading edge. I have speculated that these microscopic features are related to the lack of dynamical stability. Comparing the results of the present experiments with the structural observations made at $\psi = -0.25$ in Ref. [20] leads to the conclusion that the pinning of wide confined states does not strongly affect their spatiotemporal structure apart from making the drift velocity vanish.

The mechanism of destabilization of narrow pulses has also been the subject of previous experiments in the range $\psi \geq -0.089$ [10,13–15]. The present work extends these observations to more negative ψ, and the picture we now have is reasonably well mapped out, if not completely understood. Three mechanisms of narrow pulse destabilization have been identified. The first is destruction of the pulse by convective amplification of TW fluctuations [13]. In a cell of length Γ, the threshold for this process is found from a linear analysis to be $r_f = r_{co}(1+\varepsilon_f)$, where

$$\varepsilon_f = \frac{s\tau_0}{\Gamma} \ln \gamma_f \ . \tag{5}$$

Here s is the group velocity of small-amplitude TW's, τ_0 is the characteristic time scale for their growth [note that τ_0 is unrelated to time scale τ_o defined in Eq. (1)] [26], and γ_f is the gain factor by which naturally occurring fluctuations must be amplified in order to attain sufficient amplitude to destroy a pulse. In Ref. [13], we identified

this mechanism and estimated that $\gamma_f = 40-400$ for $\psi = -0.069$. I have measured the group velocity s for all experiments performed in this apparatus and have verified that the theoretical value $\tau_0 = 0.108$ [26] is both independent of ψ and close to the experimental value [27].

The second mechanism of pulse destabilization is the transition from a convective to an absolute instability [6,15]. The threshold for this reason is also obtained from a linear analysis and occurs at $r_a = r_{co}(1+\varepsilon_a)$, where

$$\varepsilon_a = \left[\frac{s\tau_0}{2\xi_0}\right]^2 (1+c_1^2)^{-1} . \quad (6)$$

Here, ξ_0 is the characteristic length appearing in the CGLE, and c_1 is the linear dispersion coefficient. Experiments support the theoretical results that $\xi_0 = 0.383$ is independent of ψ and that $c_1^2 \leq 0.02$ for all values of ψ under consideration here [3,15,26,27]. Because $s \propto (-\psi)^{1/2}$, the relative values of the thresholds in Eqs. (5) and (6) depend both on the cell length Γ and on ψ. Thus, by using experimental fluids with different separation ratios in rectangular cells of varying lengths, Kaplan and Steinberg [15] were able to quantitatively verify that the upper limit of pulse stability for $-0.055 \leq \psi \leq -0.005$ coincided with the smaller of the two linear thresholds r_f and r_a. For this range of separation ratios, the linear analysis correctly predicts the threshold for the destabilization of narrow TW pulses.

The third mechanism of destabilization of narrow pulses identified in Refs. [10,14] and explored herein has been termed "intrinsic destabilization." When the threshold r_1 for this process is exceeded, the pulse simply expands into the rest of the cell, accompanied by a strong decrease in the phase velocity of the underlying TW's. There is no theoretical prediction for r_1. The relationship of this process in other destabilization mechanisms is shown in Fig. 34. There, solid circles represent measurements of r_1, and solid squares show measurements of the linear onset r_{co}. The curve marked r_a shows the convective-absolute threshold in Eq. (6), evaluated using the measurements of s and r_{co} and computed values for other parameters [26]. The fluctuation threshold r_f shown in the correspondingly marked curve was obtained from Eq. (5), assuming $\Gamma = 82.47$ and $\gamma_f = 125$.

Several important points are evident in Fig. 34. First, the observation that $r_f < r_1$ for $\psi = -0.127$ and -0.072 explains why fluctuation suppression has been necessary for the observation of intrinsic destabilization of these values of ψ. Fluctuation suppression effectively erases the curve r_f from the graph, leaving r_1 as the lowest threshold for pulse destabilization. Second, while r_f depends on parameters, it can never be less than r_{co}. Thus, for $\psi \leq -0.14$, where $r_1 \leq r_{co}$, fluctuations never play a role, and intrinsic destabilization is the only possible destabilization process. Finally, $r_1 < r_a$ for all $\psi \leq -0.072$. For these ψ, the convective-absolute transition also never plays a role. The observation in Ref. [15] that, in the absence of fluctuations, this transition is the first mechanism of pulse destabilization for $\psi \geq -0.055$ may mean that $r_1 > r_a$ for this range of ψ, following the dashed extrapolation of the r_1 curve in Fig. 34. I will return to this point below, where I suggest instead that another instability inherent in the CGLE actually precedes the convective-absolute threshold and can be identified with intrinsic destabilization.

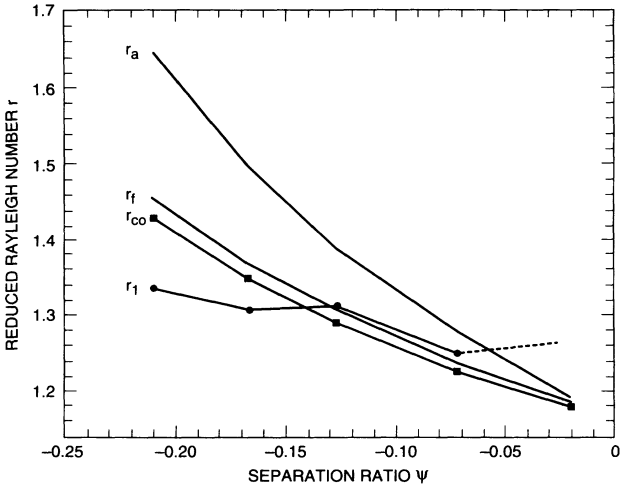

FIG. 34. Thresholds for the destabilization of narrow pulses are plotted vs separation ratio ψ. Squares show the measured threshold r_1 for intrinsic destabilization, and circles show the measured onset r_{co} for the onset of convection. The curve marked r_f is evaluated from the measurements of r_{co} using Eq. (5) and parameter values discussed in the text. The curve marked r_a is evaluated using r_{co} and Eq. (6). In the absence of fluctuations, the lowest threshold for pulse destabilization for $\psi \leq -0.072$ is r_1. The dashed extrapolation of r_1 to $\psi > -0.072$ is discussed in the text.

The final topic addressed in these experiments concerns new confined states. Two were encountered. The weakly unstable defected confined states at $\psi = -0.127$ and -0.167 were so robust that they could be characterized in detail. I speculate that the tendency of wide confined states to develop spatiotemporal defects at these separation ratios is related to the lack of stability of wide defect-free confined states. Defected confined states have also been observed in experiments in a wide rectangular cell at $\psi = -0.089$ in Ref. [14], but the presence of an end wall in those experiments makes their relationship to the present observations unclear.

It has also been possible to create transient localized states of nearly steady rolls at $\psi = -0.127$ and -0.072. These structures are strongly unstable, rapidly giving way to drifting patterns of TW's. It is not difficult to imagine why this happens: in a pattern of stationary convection rolls in a binary fluid mixture, the ethanol-concentration field is in phase with the convective velocity and temperature fields; that is, convective rolls with opposite circulation directions have equal mean ethanol concentrations [19,28]. Because of this symmetry, there can be no preferred propagation direction. However, the fundamental

reason for the existence of TW's is that this situation is unstable at sufficiently low Rayleigh numbers. Some perturbation or inhomogeneity always causes a symmetry-breaking transition to a state in which rolls with different circulation directions exhibit different mean ethanol concentrations. This is turn causes the pattern to move [29]. This effect grows weaker as ψ is made less negative, and indeed I have been able to create confined states of truly steady rolls just above onset at $\psi=-0.020$ [27]. In those experiments, it is convectively amplified TW fluctuations that destabilize the confined state, not a fundamental instability of the convective concentration field. I expect to be able to observe stable, time-independent confined states of steady convective rolls at $\psi\sim-0.01$.

The experimental results presented in this paper can be compared with those of numerical integrations of the full Navier-Stokes equations in two dimensions [19]. In these computations, a wide confined state was observed at $\psi=-0.25$ and a narrow pulse was seen at $\psi=-0.08$. The drift velocity of the narrow pulse matched the experimental observations in Ref. [12] reasonably well. Now that drifting wide confined states have been characterized, it has become apparent that the computed drift velocity does not match in this case: the numerical confined states drift forward rather than backward. This qualitative discrepancy is undoubtedly due to the influence of the narrow cell width in the experiments. The interesting qualitative issues that remain to be explored in the numerical experiments is whether narrow pulses and defected confined states at large $|\psi|$ and unstable wide confined states at small $|\psi|$ can be seen.

Theoretical work on the stability and structure of confined states is often performed using the complex Ginzburg-Landau equation. Both analytical work on simple solutions of this equation and numerical computation of more complicated solutions have been instructive. It is useful to consider how the present results can be interpreted in this context. As mentioned above, a linear analysis of this system predicts thresholds r_f and r_a for the destabilization of narrow pulses quantitatively correctly for $\psi\geq-0.055$, but this agreement does not extend to $\psi\leq-0.072$. The intrinsic destabilization seen in this range of ψ appears to be a nonlinear effect which is triggered at a lower threshold Rayleigh number. I have recently noted that the nonlinear dispersion of extended TW at $\psi=-0.127$ is also inconsistent with the predictions of the CGLE [22]. It turns out that the coupled-field model of Ref. [18] is also unstable to match the measured nonlinear dispersion [27].

If quantitative agreement with experiment is lacking, then what qualitative guidance can we expect from this model? First, it should be reiterated that the present results have established the existence of a discrete family of confined states whose drift velocity vanishes only on a measure-zero set of parameters, removing a long-standing discrepancy between old experimental observations and the properties of confined-state solutions of the CGLE [6]. Second, Riecke has shown that the inclusion of a coupled slow mode corresponding to the experimental concentration field in this model can account semiquantitatively for both the slow drift of TW pulses and for the existence of wide confined states [18]. The properties of these confined states depend on the parameters of the model in ways which may only be qualitatively related to experimental parameters. Finally, the CGLE is known to exhibit nonlinear pulse destabilization. van Saarloos and Hohenberg investigated the behavior of separated fronts, analytically computing the velocity $v^{\dagger}$ with which these move apart [6]. $v^{\dagger}$ increases nonlinearly with Rayleigh number. They verified in numerical experiments that pulses grow unstable above the threshold ε_3 determined by the condition $v^{\dagger}=0$. It is not yet clear whether this mechanism is the same as the experimentally observed intrinsic destabilization. Hakim and Pomeau [8] studied front propagation analytically, in the limit that the imaginary parts of the coefficients are small, and they studied the evolution and stability of bound pairs of widely separated fronts—the equivalent of the wide confined states in these experiments. They obtained the following equation for the evolution of the front separation w:

$$\frac{dw}{dt}=4\xi\alpha(r-r_\infty)-\frac{4}{\xi}\exp\left[-\frac{2w}{\xi}\right]+\frac{2C_2}{w}\ . \tag{7}$$

Here, α is a constant expressing the relationship between the experimental Rayleigh number and the stress parameter in the CGLE, and $r_\infty=r_o(w\to\infty)$. $\xi>0$ is a function of the real parts of the coefficients in the CGLE, and C_2 is a function of the imaginary parts. This result is easily put into the form of Eq. (1): with $\tau_o=1/4\xi\alpha$, the neutral Rayleigh number is

$$r_o(w)=r_\infty+Be^{-2w/\xi}-\frac{C}{w}\ , \tag{8}$$

where $B=1/\alpha\xi^2$ and $C=C_2/2\alpha\xi$. The stability properties discussed in Ref. [8] are equivalent to the observation in this paper that confined states are stable (unstable) if dr_o/dw is positive (negative). Confined states are unstable for all $C\leq0$. The behavior of $r_o(w)$ in Eq. (8)

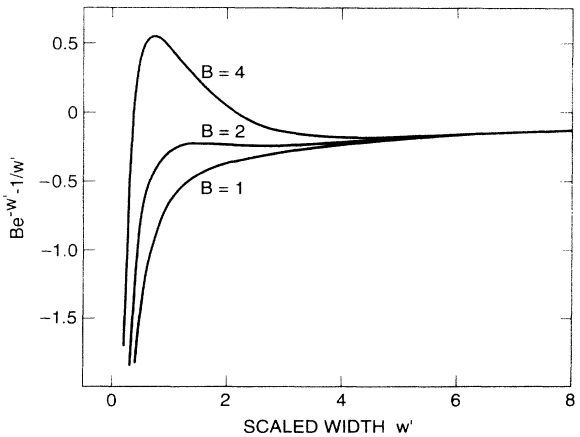

FIG. 35. The function defined in Eq. (8), taken from Ref. [8], is plotted vs the scaled width $w'=2w/\xi$, for $B=1$, 2, and 4, with $r_\infty=0$ and $C=1$. The progression of these curves as B is increased matches the qualitative trend seen in $r_o(w)$ as ψ is increased; see Fig. 32.

matches that observed in the present experiments for sufficiently small $C/B>0$, if we postulate that C/B and r_∞ are monotonic functions of ψ. To show this, I have evaluated Eq. (8) for three values of B in Fig. 35, setting $C=1$, $\xi=2$, and $r_\infty=0$ for convenience. The curves for $B=1$, 2, and 4 bear a good qualitative resemblance to the curves for $\psi=-0.210$, -0.167, and -0.127, respectively, in Fig. 32, modulo the Rayleigh-number offset and width scaling [30]. It remains to be shown, of course, that this correspondence between B and ψ is physically correct.

Thus the CGLE exhibits a nonlinear pulse destabilization mechanism which at least qualitatively matches the experimental observations. It is not yet clear whether the numerical front expansion observed in Ref. [6] is identical with or even related to the evolution described analytically in Eq. (8). This relationship, as well as a comparison of both nonlinear thresholds with the convective-absolute instability threshold, would be quite interesting to explore. It would also be worthwhile to investigate this issue using the coupled-field model of Ref. [18]; work on this topic has recently begun [31].

ACKNOWLEDGMENTS

I am pleased to acknowledge continuing conversations with P. C. Hohenberg and H. Riecke.

[1] E. Moses, J. Fineberg, and V. Steinberg, Phys. Rev. A **35**, 2767 (1987); R. Heinrichs, G. Ahlers, and D. S. Cannell, *ibid.* **35**, 2761 (1987).

[2] P. Kolodner, D. Bensimon, and C. M. Surko, Phys. Rev. Lett. **60**, 1723 (1988); D. Bensimon, P. Kolodner, C. M. Surko, H. Williams, and V. Croquette, J. Fluid Mech. **217**, 441 (1990).

[3] P. Kolodner, C. M. Surko, and H. Williams, Physica D **37**, 319 (1989); V. Steinberg, J. Fineberg, E. Moses, and I. Rehberg, *ibid.* **37**, 359 (1989).

[4] V. Steinberg, E. Moses, and J. Fineberg, Nucl. Phys. B (Proc. Suppl.) **2**, 109 (1987); K. Lerman, E. Bodenschatz, D. S. Cannell, and G. Ahlers, Phys. Rev. Lett. **70**, 3572 (1993).

[5] O. Thual and S. Fauve, J. Phys. (Paris) **49**, 1829 (1988); O. Thual and S. Fauve, Phys. Rev. Lett. **64**, 282 (1990).

[6] W. van Saarloos and P. C. Hohenberg, Phys. Rev. Lett. **64**, 749 (1990); Physica D **56**, 303 (1992); **69**, 209(E) (1993).

[7] V. Hakim, P. Jakobsen, and Y. Pomeau, Europhys. Lett. **11**, 19 (1990); B. A. Malomed and A. A. Nepomnyashchy, Phys. Rev. A **42**, 6009 (1990).

[8] V. Hakim and Y. Pomeau, Eur. J. Mech. B **10**, 137 (1990).

[9] J. J. Niemela, G. Ahlers, and D. S. Cannell, Phys. Rev. Lett. **64**, 1365 (1990).

[10] P. Kolodner, Phys. Rev. A **44**, 6448 (1991).

[11] V. Steinberg and E. Kaplan, in *Proceedings of the NATO Advanced Research Workshop on Spontaneous Formation of Space-Time Structures and Criticality,* edited by T. Riste and D. Sherrington (Kluwer, Dordrecht, 1991), p. 207.

[12] P. Kolodner, Phys. Rev. Lett. **66**, 1165 (1990).

[13] P. Kolodner and J. A. Glazier, Phys. Rev. A **42**, 7504 (1990); J. A. Glazier and P. Kolodner, *ibid.* **43**, 4269 (1991).

[14] P. Kolodner, Phys. Rev. A **43**, 2827 (1991).

[15] E. Kaplan and V. Steinberg, Phys. Rev. A **46**, 2996 (1992).

[16] P. Kolodner, Phys. Rev. A **44**, 6466 (1991).

[17] H. R. Brand and R. J. Deissler, Phys. Rev. Lett. **63**, 2801 (1989); R. J. Deissler and H. L. Brand, Phys. Lett. A **146**, 252 (1990).

[18] H. Riecke, Phys. Rev. Lett. **68**, 301 (1992); Physica D **61**, 253 (1992).

[19] W. Barten, M. Lücke, and M. Kamps, Phys. Rev. Lett. **66**, 2621 (1991); M. Lücke, W. Barten, and M. Kamps, Physica D **61**, 183 (1992).

[20] C. M. Surko, D. R. Ohlsen, S. Y. Yamamoto, and P. Kolodner, Phys. Rev. A **43**, 7101 (1991).

[21] P. Kolodner, Phys. Rev. E **48**, 4187 (1993).

[22] P. Kolodner, Phys. Rev. A **46**, 6431 (1992); **46**, 6452 (1992).

[23] P. Kolodner and H. Williams, in *Proceedings of the NATO Advanced Research Workshop on Nonlinear Evolution of Spatio-Temporal Structures in Dissipative Continuous Systems,* Vol. 225 of *NATO Advanced Study Institute, Series B: Physics,* edited by F. H. Busse and L. Kramer (Plenum, New York, 1990), p. 73.

[24] P. Kolodner, H. Williams, and C. Moe, J. Chem. Phys. **88**, 6512 (1988).

[25] In previous publications, Rayleigh numbers have been quoted in terms of the fractional distance ε above the onset of convection. In order to preserve the relationship of the present work with the extended-state experiments in Ref. [22], I translate previous results into absolute Rayleigh numbers in this paper.

[26] M. C. Cross and K. Kim, Phys. Rev. A **37**, 3909 (1988).

[27] P. Kolodner (unpublished).

[28] K. D. Eaton, D. R. Ohlsen, S. Y. Yamamoto, C. M. Surko, W. Barten, M. Lücke, M. Kamps, and P. Kolodner, Phys. Rev. A **43**, 7105 (1991); B. L. Winkler and P. Kolodner, J. Fluid Mech. **240**, 31 (1992).

[29] R. W. Walden, P. Kolodner, A. Passner, and C. M. Surko, Phys. Lett. **55**, 496 (1985).

[30] At first glance, the discussion of stability in Ref. [8] appears to contradict the present experimental observations, because its authors speak of an unstable narrow pulse and a stable wide pulse. The key to this apparent disagreement is that Pomeau and Hakim do not discuss the stable pulse seen for $w'\lesssim 1$ in Fig. 35. Thus their unstable, narrow pulse refers to the region $1\lesssim w'\lesssim 3$ in the $B=4$ curve in Fig. 35; this corresponds to the unstable pulse observed for $w\gtrsim 6$ at $\psi=-0.127$. Their stable wide pulse, which should exist at all ψ because $dr_o/dw>0$ at very large w for all $B,C>0$ in Eq. (8), appears to correspond to confined-state widths that are much larger than those studied in these experiments.

[31] H. Herrero-Sanz and H. Riecke (private communication).

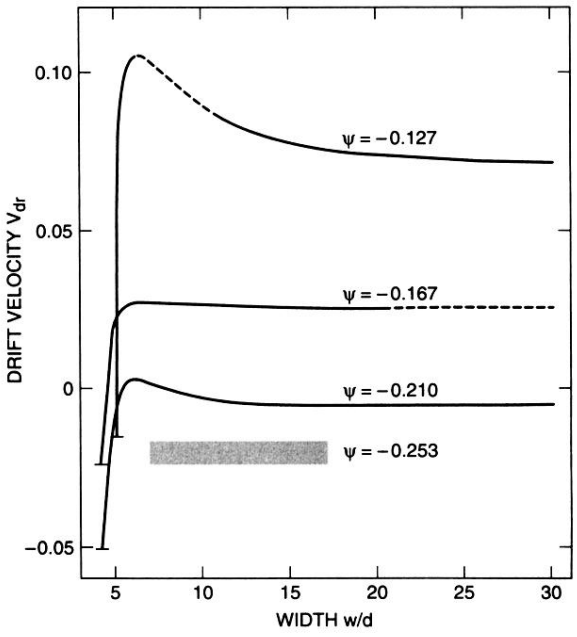

FIG. 33. The solid curves represent the measurements of the width dependence of the drift velocity of defect-free confined states at $\psi = -0.127$, -0.167, and -0.210 which exhibit zero expansion velocity. As in Fig. 32, dashed segments indicate extrapolated and interpolated values. Drift-velocity measurements at $\psi = -0.253$, whose dependence on expansion velocity has not been carefully studied, are represented by the shaded rectangle.